

Cross-Correlation of spectroscopic and photometric galaxy surveys: cosmology from lensing and redshift distortions

Enrique Gaztañaga¹, Martin Eriksen¹, Martin Crocce¹, Francisco J. Castander¹, Pablo Fosalba¹, Pol Martí², Ramon Miquel^{2,3}, Anna Cabré⁴

¹*Institut de Ciències de l'Espai (IEEC-CSIC), E-08193 Bellaterra (Barcelona), Spain*

²*Institut de Física d'Altes Energies (IFAE), E-08193 Bellaterra (Barcelona), Spain*

³*Institució Catalana de Recerca i Estudis Avançats (ICREA), E-08010 Barcelona, Spain*

⁴*University of Pennsylvania, Philadelphia, USA*

3 December 2024

ABSTRACT

Cosmological galaxy surveys aim at mapping the largest volumes to test models with techniques such as cluster abundance, cosmic shear correlations or baryon acoustic oscillations (BAO), which are designed to be independent of galaxy bias. Here we explore an alternative route to constrain cosmology: sampling more moderate volumes with the cross-correlation of photometric and spectroscopic surveys. We consider the angular galaxy-galaxy autocorrelation in narrow redshift bins and its combination with different probes of weak gravitational lensing (WL) and redshift space distortions (RSD). Including the cross-correlation of these surveys improves by factors of a few the constraints on both the dark energy equation of state $w(z)$ and the cosmic growth history, parametrized by γ . The additional information comes from using many narrow redshift bins and from measurement of galaxy bias with both WL and RSD, breaking degeneracies that are present when using each method separately. We show forecasts for a joint $w(z)$ and γ figure of merit ($\text{FoM}_{w\gamma}$) using linear scales over a deep ($i_{AB} < 24$) photometric survey and a brighter ($i_{AB} < 22.5$) spectroscopic or very accurate (0.3%) photometric redshift survey. Magnification or shear in the photometric sample produce $\text{FoM}_{w\gamma}$ that are of the same order of magnitude of those of RSD or BAO over the spectroscopic sample. However, the cross-correlation of these probes over the same area yields a $\text{FoM}_{w\gamma}$ that is up to a factor 100 times larger. Magnification alone, without shape measurements, can also be used for these cross-correlations and can produce better results than using shear alone. For a spectroscopic follow-up survey strategy, measuring the spectra of the foreground lenses to perform this cross-correlation provides 5 times better $\text{FoM}_{w\gamma}$ than targeting the higher redshift tail of the galaxy distribution to study BAO over a 2.5 times larger volume.

1 INTRODUCTION

Weak gravitational lensing is a unique tool to study the large scale dark matter distribution. The correlated shear measurements (i.e. shear-shear correlation function) provide direct information on the power spectrum of matter fluctuations (see Bartelmann & Schneider 2000, Refregier 2003, Bernstein 2009 for a review), avoiding the problem of bias, i.e. of how light traces the mass. The drawbacks are that the information is projected on the sky over a very broad radial kernel, and that the signal-to-noise is quite poor on small scales. For the former, shear-shear tomography can be of some help, but the radial precision is still typically

limited to a few redshift bins (e.g. see Hu 1999, Hu & Jain 2004, Refregier et al. 2011). For the latter we would need to measure shear for fainter magnitudes and, from the ground, this is limited by the atmospheric PSF distortion. Cosmic shear also suffers from systematic difficulties, such as shape measurement errors, the galaxy intrinsic alignment and photo-z errors. Here we will explore the combination and cross-correlation of weak-lensing probes with the 3D information in the (foreground) large scale galaxy distribution in order to complement and extend the constraining power of weak lensing and clustering measurements. The galaxy-shear cross-correlation can also be used to measure galaxy

bias. Once bias is known, we can recover the full 3D matter clustering from the 3D galaxy clustering.

We pay special attention to cosmic magnification as an alternative or complementary probe to shear. Lensing changes the area of the background image, which can result in density fluctuations in the background sources that are correlated with the density fluctuations in the foreground lenses. The resulting galaxy-galaxy cross-correlation is called cosmic magnification and contains very similar cosmological information to that provided by shear. Magnification will be compared with galaxy-shear (e.g. Johnston et al. 2007) and shear-shear as a reference (see e.g. Van Waerbeke 2009, Bernstein 2009, Van Waerbeke et al. 2010 and references therein). Cosmic magnification has long been investigated as a potential source for the puzzling galaxy-QSO cross-correlation (see Gaztanaga 2003 and references therein). Thanks to the improvements in photometric homogeneity in the SDSS sample, magnification has been detected in the cross-correlation of foreground photometric SDSS galaxies with both spectroscopic quasars (Scranton et al. 2005) and Lyman break galaxies (Hildebrandt, van Waerbeke & Erben 2009). In our approach, we envision that, in contrast to these current detections, in the near future the lensing sample should be the one with the highest radial resolution, i.e. spectroscopic or with very good (0.3%) photo- z error. For the background sources we do not need such good radial resolution to predict the lensing response. This will be ideal for 3D power spectrum reconstruction, as will be shown here.

Jain & Taylor (2003) and Bernstein & Jain (2004) proposed the use of photometric redshift data to produce a template map of foreground galaxies to cross-correlate with the induced shear as a function of the background (or source) galaxy redshift. They considered the ratios of this cross-correlation to recover the geometrical ratios rather than trying to do a full 3D tomography. Bernstein & Jain (2004) called this cross-correlation cosmography. This is related to our approach here. The common advantage in both cross-correlation techniques is that galaxy-shear cross-correlation is less sensitive than shear-shear to systematic errors in the PSF correction. The main differences with what we do here is that we consider direct cross-correlations, rather than using a template, over spectroscopic or very good photometric foreground galaxies using narrow bins. We also include cosmic magnification, restrict to linear scales (to avoid the uncertainties in galaxy power spectrum), and use the full signal (rather than just ratios). This allows to recover cosmological information in the 3D power spectrum as well as recovery of the geometrical information in lensing efficiency (see §3).

As a new ingredient, we also consider the information contained in redshift space distortions (RSD). On linear scales, galaxy (peculiar) velocities can be measured by comparing radial to transverse correlations and this provides a measurement of the linear growth rate of dark matter fluctuations. A challenge and opportunity in our approach is the need to model galaxy biasing which affects both RSD and WL cross-correlations, but in different ways. In real space, or for transverse modes, on linear scales, the galaxy auto-

correlation depends on the square of bias, the galaxy-shear cross-correlation only depends linearly on bias and shear-shear is independent of bias. This means that their combination can be used to measure bias as well as the growth information (e.g. see Hoekstra et al. 2002 and §2.4 below). In redshift space, i.e. for radial modes, bias only affects the density growth but not the velocity growth (e.g. see Eq.24 below), which provides an alternative route to separate growth from bias. We will show here that the combination of WL probes and RSD results in a very accurate determination of bias, also breaking the degeneracy of growth with cosmic expansion. Thus, we will combine three different types of probes here:

- Angular clustering from galaxy-galaxy autocorrelation in narrow redshift bins (which we call G-G)
- WL from shear-shear (S-S), galaxy-shear (G-S) or magnification (MAG, i.e. galaxy-galaxy cross-correlation)
- RSD, from the ratio of transverse to radial modes.

The importance of combining redshift space distortions and weak lensing information to test cosmological models and modified gravity has been highlighted by several authors (e.g. Zhang et al. 2007, Guzik, Jain & Takada 2010, Song et al. 2011 and references therein). Recently, Reyes et al. (2010) used this combination to measure the growth of structure from a ratio of galaxy-galaxy auto-correlation with galaxy-shear cross-correlation in combination with RSD. Here we will see how this can be generalized when you use all the information, not only the ratios, and have many redshifts bins with much better radial resolution. Potentially RSD could benefit from the combination of samples with different biases over the same region of sky (McDonald & Seljak 2009). This effect is also included in our analysis as we will consider bright and faint galaxy populations with different biases. But this has little effect on our forecast for the particular surveys we are modeling. It might also be possible to exploit this further by further division of the galaxy population or direct lensing calibration of biasing (Bernstein & Cai 2011).

Cross-correlation of photometric and spectroscopic samples in the same redshift bin can also be used to estimate photometric redshift contamination and determining the redshift distribution of the photometric sample (e.g. Newman 2008). This technique will be generalized here to the cross-correlation between separate bins by inclusion of transition probabilities r_{ij} .

A motivation for our study has been the science case for the PAU Survey (www.pausurvey.org) based on the PAU Camera (PAUCam, Casas et al. 2010) a photometric camera with 40 narrow (100Å) filters and 6 broad band filters that will be commissioned at WHT Telescope in La Palma at the end of 2012. PAUCam can map about 2 deg² of the sky each night with all these filters producing an imaging survey to a depth of about $i_{AB} \simeq 24$. Because of the narrow band filters, galaxies with $i_{AB} < 22.5$ will have a photo- z accuracy of about 0.35% (i.e. about 10 Mpc/h), while the accuracy for the rest of the galaxies is about 3% (both with around 50% completeness for all type of galaxies). The bright sample will be much denser (~ 15000 galaxies per deg²) than

RSD	Redshift Space Distortions
WL	Weak Lensing
BAO	Baryon Acoustic Oscillations
G-G	Galaxy-Galaxy auto-correlation
MAG	Magnification from G-G auto and cross-correlation
S-S	Shear-Shear correlations
G-S	Galaxy-Shear correlations
WL-all	combination of S-S, G-S, G-G and MAG
F	Fain sample of galaxies $22.5 < i_{AB} < 24$
B	Bright sample of galaxies $i_{AB} < 22.5$
F+B	Combination of independent F and B samples
FxB	Cross-correlation of F and B over same area

Table 1. Notation and acronyms used in this paper.

any spectroscopic surveys to the same depth. Unlike most spectroscopic surveys, which target predetermined galaxies, PAU will also be blind in that it will contain all the objects in the surveyed area to a given brightness. In our initial studies for PAUCam, we only explored BAO with $i_{AB} < 22.5$ LRG galaxies (Benitez et al. 2009). However, as we discuss next, this is a rather restrictive use for the PAUCam data. A similar approach has been taken by several spectroscopic surveys which plan to measure BAO at high redshifts by selecting appropriate spectroscopic targets out of a given parent photometric catalog. Here we will consider forecasts using both the faint photometric and bright (quasi) spectroscopic samples and we will show that one can get significantly better cosmological constraints when using probes based on the combination of WL and RSD.

We will consider both a modest 200 deg² PAU-like Survey and a more ambitious 5000 deg² survey. Such a survey could also result from the Dark Energy Survey (DES), which will image 5000 deg² in five passbands to 24th mag over 5 years starting in 2012, producing weak lensing shape measurements for about 200 million galaxies. A massive follow-up spectroscopic survey over a substantial part of the DES footprint, e.g., using multi-fiber spectrographs such as BigBOSS or DESpec, would enable RSD measurements of the lensing population and the implementation of this cross-correlation technique. Unlike BAO or supernovae, WL and RSD can also provide very valuable information on cosmic growth history and this is a key ingredient to understand the physics of the accelerating universe.

This paper is organized as follows. In §2 we present the modeling, methodology and different assumptions used. We include a subsection on how we model galaxy bias and another one on modeling of redshift space distortions. Section 3 describes the approximations we make for weak gravitational lensing. The reader familiar with these techniques can directly jump to §4, where we present our fiducial surveys. In §5 we present results of our forecast as a function of the different ingredients, to disentangle the different contributions to the FoM. This section could also be skipped if the reader is not interested in such details. In §6 we present the main result in this paper, i.e. the comparison of forecasts for different surveys. We finish in §7 with some conclusions and summary of the main results. Table 1 summarizes the notation that will be used in this paper.

2 MODELING

In this section we will introduce the different assumptions and modeling used in this paper. Section 2.1 and 2.2 introduce the cosmological model and the parameters that we want to study. In Section 2.3 we present the Fisher Matrix approach and the figures of merit that will be used to compare experiments. Sections 2.4 and 2.5 present and justify the models for galaxy bias and redshift space distortions.

2.1 Growth and Cosmic History

The cosmic expansion history, $a = a(t)$ or $H = H(t)$, in a flat FLRW background with matter density ρ_m and dark energy (DE) equation of state $w = p_{DE}/\rho_{DE}$, can be written as:

$$H^2 \equiv \left(\frac{\dot{a}}{a}\right)^2 = \frac{8\pi G}{3}(\rho_m + \rho_{DE}) - \frac{k}{a^2} \quad (1)$$

$$= H_0^2 \left[\Omega_m a^{-3} + \Omega_k a^{-2} + \Omega_{DE} a^{-3(1+w)} \right]$$

where $\Omega_k = 1 - \Omega_m - \Omega_{DE}$ measures deviations from flat curvature $k = 0$ and we have neglected radiation. Our fiducial model corresponds to Λ CDM: a flat universe with $w = -1$, so that the DE density is constant with redshift z . We will explore how well our different observational probes can constraint w and its variation $w = w(z)$.¹ Parameters w_0 and w_a are used to characterize the evolution of DE equation of state (Chevallier & Polarski 2001, Linder 2003):

$$w(z) = w_0 + w_a(1 - a) = w_0 + w_a z / (1 + z) \quad (2)$$

According to General Relativity (GR), given this cosmic history, the equations that determine the growth history, i.e. the cosmic evolution of the linear density contrast δ , are of the form (Peebles 1980; Bernardeau et al. 2002)

$$\ddot{\delta} + 2H\dot{\delta} = 4\pi G\rho_m\delta \quad (3)$$

with the solution

$$\delta = D(a)\delta(0) \quad (4)$$

where the growth factor $D(a)$ depends on the expansion history $H(a)$ (through $w(a)$) and in $\Omega_m(a)$. Any discrepancy found between the observed growth and the growth D predicted for a given expansion history H can be used as a test for modifications to GR or variations on the cosmological model. This linear growth can also be characterized by its derivative, the velocity growth factor:

$$f \equiv \frac{d \ln D}{d \ln a} = \frac{\dot{\delta}}{\delta} \equiv \Omega_m^\gamma(a) \quad (5)$$

where γ is the gravitational growth index (see Linder 2005). So when normalized to $D = 1$ today, then

$$D(a) = \exp \left[- \int_a^1 d \ln a f(a) \right] \quad (6)$$

¹ When $w = w(z)$ we need replace w in $\Omega_{DE} a^{-3(1+w)}$ in Eq. 1 by the corresponding integral over redshift.

For GR with DE equation of state w , Linder (2005) finds that to a good approximation:

$$\gamma \simeq \frac{3(w-1)}{6w-5} \quad (7)$$

This reduces to the well known result $\gamma \simeq 0.55$ for Λ CDM ($w = -1$). Thus for DE models in GR, measurements of $f(z)$ can be used to estimate $w(z)$, independently from measurements of $H(z)$. Other cosmological models have a different relation between $D(z)$ and $H(z)$ (e.g. see Gaztanaga & Lobo 2001) which results in different effective values for γ . For example, in the DGP model $\gamma \simeq 0.68$ (Lue, Scoccimarro & Starkman 2004). More generically, an independent measurement of γ and w can be related to a measurement of time variations of Newton's constant G (e.g. see Eq.32 in Pogosian et al. 2011), which provides a direct test of GR. This will be our approach here: we will check how well we can measure separately w and γ with different probes, assuming they are independent of each other. We will not make use of GR to relate cosmic growth to cosmic history (i.e. we will not use Eq.7 or Eq.3), but rather we will use a parametric description in terms of independent parameters: w_0 , w_a and γ (plus the standard cosmological parameters in Eq.9 below). This can be used to separate GR from other theories of gravity and learn about the nature of the accelerated expansion.

2.2 Fiducial Cosmological model

To characterize cosmic history and the linear matter power spectrum, we use the standard set of 8 cosmological parameters (e.g. see Komatsu et al. 2011):

$$w_0, w_a, h, n_s, \Omega_m, \Omega_B, \Omega_{DE}, \sigma_8 \quad (8)$$

In addition, the growth index in Eq.5 is allowed to vary independently of $w(z)$ to characterize the growth history and to test Modified Gravity separately from DE evolution. To model bias we include an additional set of independent bias parameters as described later on in §2.4. Thus we have a total of 9 cosmological parameters together with some nuisance bias parameters b_i :

$$p_\nu = (w_0, w_a, h, n_s, \Omega_m, \Omega_B, \Omega_{DE}, \sigma_8, b_i, \gamma). \quad (9)$$

Note that in general $\Omega_k = 1 - \Omega_m - \Omega_{DE}$ differs from zero. For the fiducial values we use $w_0 = -1$, $w_a = 0$, $h = 0.7$, $n_s = 0.95$, $\Omega_m = 0.25$, $\Omega_B = 0.044$, $\Omega_{DE} = 0.75$, $\sigma_8 = 0.8$, $\gamma = 0.55$ (corresponding to its value in GR). Unless stated otherwise, results are always presented with priors from Planck and Stage-II Supernovae (SN-II)², but with no priors in γ or bias b_i .

² We use the Dark Energy Task Force (DETF) Planck and SN-II priors Fisher Matrices given in <http://www.physics.ucdavis.edu/DETFast/>, with file names `planckfish` and `SN-II`. The Planck prior on σ_8 assumes a GR model for linear growth but there are several other ways to measure σ_8 that could produce similar priors without such assumption. The actual priors and how they were obtained are somewhat irrelevant here, they just represent a baseline to compare different experiments.

Note that for completeness we include $\sigma_8 \equiv \sigma_8(0)$, the global normalization of the amplitude of density fluctuations at $z = 0$. Our goal is not to measure σ_8 but rather the evolution of this amplitude with time, i.e. $D(z)$, which is given by γ . In our analysis, σ_8 is dominated by the priors above (around 1%) as our probes are more sensitive to relative than to absolute variations. One could also try to measure σ_8 and other parameters, such as neutrino masses, by including the amplitude of CMB temperature fluctuations at $z=1100$ rather than using priors of σ_8 (i.e. at $z = 0$). This is a very different approach and involves other complications. In such case γ and σ_8 could be strongly correlated. But this is not our approach here. Our goal is to test the best way to measure cosmic and growth evolution starting from some priors at $z = 0$.

2.3 Fisher Matrix and Figures of Merit

Throughout this paper we will employ the formalism based on the Fisher Matrix (FM, Fisher 1935, Tegmark et al. 1998):

$$F_{\mu\nu} = \sum_{\ell \text{ or } k} \sum_{ij, mn} \frac{\partial C_{ij}}{p_\mu} \Theta_{ij;mn}^{-1} \frac{\partial C_{mn}}{p_\nu} \quad (10)$$

where p_ν are the cosmological parameters, nuisance parameters or additional quantities we want to forecast and C_{ij} are the observables with Θ covariance. The indices ij refer here to each pair of redshift bins and ℓ or k refers to angular scales: multipole or Fourier modes. The elements of $F_{\mu\nu}^{-1}$ are the covariance of p_μ and p_ν . For a given experiment, the FM approach is a mapping (or transformation) of the covariance in the observables to the covariance in the quantities we want to measure.

Here we will model the weak lensing (WL) probes, i.e. shear-shear, galaxy-shear and galaxy-galaxy angular correlations, in real space and using the Limber approximation (see §3.2). In this case the observables C_{ij} will be the power spectrum of the angular cross-correlations between two redshift bins. Redshift bins which will be taken to be independent, as they are separated and non overlapping in space. This means that there are no intrinsic radial correlations and we only consider transverse modes for angular clustering and WL probes. For redshift space distortions (RSD) we will use the ratio of the amplitudes of the 3D power spectrum as we change from transverse to radial modes within a single redshift bin, i.e. μ in Eq.24. We neglect the covariance between these ratios and the transverse angular power spectrum. When RSD is combined with BAO we also neglect the covariance between the RSD ratios and the BAO wiggles. In linear theory, these covariances are negligible because sampling variance cancels in the ratios. Hence the combination of RSD with the WL probes or BAO is given by the addition of the corresponding Fisher matrices.

2.3.1 Non-linear scales

The FM depend on scales³ as the summation is over all scales that contribute to the analysis in Eq. (10). If we fix a minimum scale R_{min} defined by the validity of “linear” theory today, the redshift evolution of R_{min} can be obtained through this relation:

$$\sigma(R_{min}, z) = 1 \quad (11)$$

where $\sigma(R, z) = \int P_L(k, z) W^2(kR) d^3k$ is the amplitude of fluctuations on scale R , $W(x) = \exp(-x^2/2)$ is a Gaussian smoothing kernel and $P_L(k, z)$ is the linear matter power spectrum. These are the same criteria adopted by White et al. 2009. The maximum k -mode is then given by

$$k_{max}(z) = k_{max} \frac{R_{min}(0)}{R_{min}(z)} h \text{Mpc}^{-1} \quad (12)$$

with $k_{max} = 0.1$ to “normalize” this scale to $0.1 h \text{Mpc}^{-1}$ at $z = 0$. The corresponding maximum ℓ -mode is given by

$$\ell_{max} + 1/2 = k_{max}(z_i) r(z_i) \quad (13)$$

where r is the transverse comoving distance to the redshift bin i under consideration. In the forecast, we consider cross-correlations to scales up to the ℓ_{max} of the closest bin (i.e. the smallest ℓ_{max} of the two bins). For the maximum scale we use $k_{min} = 0.001 h \text{Mpc}^{-1}$ for all z and $l_{min} = 50$ to avoid inaccuracies in the Limber approximation⁴.

These conditions, in Eq.(11)-(12), yield very similar values for k_{max} to those found by studying the limitations of perturbation theory by Jeong & Komatsu 2006 (see also Jeong & Komatsu 2009). In this analysis we will only use linear theory for $P(k)$ and Gaussian initial conditions.

2.3.2 Figures of Merit

In the FM approach the marginalized 1-sigma variance in parameter p_ν is given by the diagonal element of the inverse of the FM: $\sigma^2(p_\nu) = [F^{-1}]_{\nu\nu}$. When optimizing an experiment with more than one parameter, you need to take into account their covariance. We will then cast our results in terms of:

$$\text{FoM}_S = \sqrt{\frac{1}{\det[F^{-1}]_S}}, \quad (14)$$

where S is the sub-space of parameters we are interested on. For just one parameter, this is the inverse error, for two this is proportional to the inverse area included within the 1-sigma error ellipse (Albrecht et al. 2006), for three this is the inverse volume within the 1-sigma error ellipsoid, and so on. In this paper, we will focus on three different figures of merit:

- FoM_w : Constraints on (w_0, w_a) marginalizing over the remaining cosmological and bias parameters, similar to the

³ We employ spherical coordinates in the formalism of weak lensing (i.e. ℓ -modes) and f modes for RSD (i.e. k -modes).

⁴ Notice that error-bars are larger at large scales, hence this choice has little impact on FM constraints.

DETF FoM (Albrecht et al. 2006). But note how here we allow γ to vary, while in Albrecht et al. (2006) this figure of merit is quoted for a fixed value of $\gamma \simeq 0.55$ corresponding to GR.

- FoM_γ : the inverse of the achievable 1-sigma error in γ after marginalization over the remaining parameter space.
- $\text{FoM}_{w\gamma}$: Joint constraint on (w_0, w_a, γ) , a natural extension to the dark energy FoM of the DETF.

We find that there is little covariance between γ and (w_0, w_a) , which means that $\text{FoM}_{w\gamma} \simeq \text{FoM}_\gamma \times \text{FoM}_w$. Note that the above definitions have different dimensions since they involve different numbers of parameters. To have a direct comparison of the (geometrical) mean error in the different cases we should compare FoM_w to FoM_γ^2 and $\text{FoM}_{w\gamma}^{2/3}$.

2.4 Galaxy Bias and its cross-correlation

In this section we will justify how we model galaxy bias. This is a key ingredient in our approach as both RSD and WL cross-correlations depend on bias. We will show that we do not need to include a correlation coefficient between galaxy and matter cross-correlations, and argue that we only need to allow bias to vary on time scales larger than $\Delta a \simeq 0.1$.

2.4.1 Bias stochasticity and scale dependence

In the local bias model (Fry & Gaztanaga 1993), the smoothed galaxy fluctuation δ_g at a point \vec{x} is a function of the matter field δ_m at the same point. For small fluctuations we can Taylor-expand this function and approximate the local bias model as:

$$\delta_g(\vec{x}, z) = b(z) \delta_m(\vec{x}, z) \quad (15)$$

The galaxy-galaxy (auto) correlation $\xi_{gg} = \langle \delta_g \delta_g \rangle$ and galaxy-mass (cross) correlation $\xi_{gm} = \langle \delta_g \delta_m \rangle$ are then:

$$\begin{aligned} \xi_{gg}(s, z) &= b^2(z) \xi_{mm}(s, z) \propto b^2(z) D^2(z) \\ \xi_{gm}(s, z) &= b(z) \xi_{mm}(s, z) \propto b(z) D^2(z) \end{aligned} \quad (16)$$

where $\xi_{mm}(r)$ is the matter-matter correlation and $s \equiv |\vec{x}_2 - \vec{x}_1|$ is the separation between pairs and the second step uses the linear gravitational growth. Under these linear and local assumptions one can combine ξ_{gg} and ξ_{gm} to break the degeneracy between b and D . A more general parametrization of bias is based on the cross-correlation coefficient, R , defined as:

$$r \equiv \frac{\xi_{gm}}{\sqrt{\xi_{gg}\xi_{mm}}} \quad (17)$$

If instead of using the local bias model we assume an effective bias $\bar{b}^2 \equiv \xi_{gg}/\xi_{mm}$ that is constant as a function of scale we find:

$$\begin{aligned} \sqrt{\xi_{gg}/\xi_{mm}} &= \bar{b}(z) \\ \xi_{gm}/\xi_{mm} &= \bar{b}(z) r(z) \\ \xi_{gg}/\xi_{gm} &= \frac{\bar{b}(z)}{r(z)} \end{aligned} \quad (18)$$

where $r(z)$ can differ from unity (e.g. see Tegmark & Peebles 1998, Pen 1998, Dekel & Lahav 1999, Casas-Miranda et al 2002, Seljak & Warren 2004, Bonoli & Pen 2009). In the local model $r(z) = 1$ and all these ratios are just equal. It is still possible to measure $D(z)$, $b(z)$ and $r(z)$ using more observables, such as ξ_{mm} from shear-shear or $P(k, \mu)$ from redshift space distortions.

We will show next that on large scales, when \bar{b} is constant as a function of scale, r has to be close to unity and there is no need to introduce this parameter. Let us add nonlinearities and a stochastic component $\epsilon(\vec{x}, z)$ which could be caused by shot-noise or non-local perturbations:

$$\delta_g(\vec{x}, z) = b_1(z) \delta_m(\vec{x}, z) + b_2(z) \delta_m^2(\vec{x}, z) + \epsilon(\vec{x}, z) \quad (19)$$

By definition, ϵ is not correlated to δ_m . Otherwise, the correlated part will just renormalize b_1 and b_2 . Then

$$\begin{aligned} \xi_{gg} &= b_1^2 \xi_{mm} + \xi_\epsilon + 2b_1 b_2 \xi_3 + b_2^2 \xi_4 \\ \xi_{gm} &= b_1 \xi_{mm} + b_2 \xi_3 \end{aligned} \quad (20)$$

where we have introduced $\xi_\epsilon \equiv \langle \epsilon \epsilon \rangle$, $\xi_3 \equiv \langle \delta_m \delta_m^2 \rangle$ and $\xi_4 \equiv \langle \delta_m^2 \delta_m^2 \rangle$ for the 3 and 4 point correlations. All these new correlations have a different scale dependence on the separation s than $\xi_{gg}(s)$. For Gaussian initial conditions: $\xi_3 \simeq \xi_{mm}^2$ and $\xi_4 \simeq \xi_{mm}^3$ (see Bernardeau et al. 2002). On large scales, $s > 10Mpc/h$, where $\xi_{mm} < 1$:

$$\xi_{gg} \simeq b_1^2 \xi_{mm} + \xi_\epsilon = b_1^2 \xi_{mm} \left(1 + \frac{\xi_\epsilon}{b_1^2 \xi_{mm}}\right) \quad (21)$$

$$\begin{aligned} \xi_{gm} &\simeq b_1 \xi_{mm} \\ r &\simeq \frac{1}{\sqrt{1 + \xi_\epsilon / b_1^2 \xi_{mm}}} \simeq 1 - \frac{\xi_\epsilon}{2b_1^2 \xi_{mm}} \end{aligned} \quad (22)$$

In general $\xi_\epsilon(s) \ll \xi_{mm}(s)$ and the above equations reproduce the local bias results in Eq.16 with $b = b_1$, even when the stochastic ϵ can be shown to be quite large, even larger than δ_m (see Fig.1 in Manera & Gaztanaga 2011). When $\xi_\epsilon(s)/\xi_{mm}(s)$ is not negligible then we have that r is scale dependent, since both ξ_ϵ and ξ_{mm} depend on the pair separation s . But, in such a case the effective bias, defined as $\bar{b}^2 = \xi_{gg}/\xi_{mm}$, will also depend on scale. In other words, whenever the effective bias \bar{b} is independent of scale, Eq.21 indicates that we can neglect the scale dependent terms, i.e. $\xi_\epsilon/b_1^2 \xi_{mm}$ and then, according to Eq.22, we force $r \simeq 1$. This result is well reproduced in halo bias simulations on scales $s > 20Mpc/h$ (see Fig.4 and Fig. 13 in Manera & Gaztanaga 2011 and next sub-section).

Seljak & Warren 2004 and Bonoli & Pen 2009 found that r tends to unity on large scales in halos in numerical simulations but deviations from $r = 1$ are significant even on the largest scales. It should be noted that these references studied $r(k)$ in Fourier and not in configuration space. In Fourier space r is also subject to shot-noise, because r is build from the power spectra $\langle \delta(k)^2 \rangle$, while shot-noise cancels for the correlation $\langle \delta(r)\delta(r') \rangle$. Correcting for shot-noise of halos is possible but complicated as halos have a exclusion region which results in a sub-Poisson correction (see Casas-Miranda et al 2002, Manera & Gaztanaga 2011). Below we will explore how close r is to unity in numerical simulations and as a function of redshift.

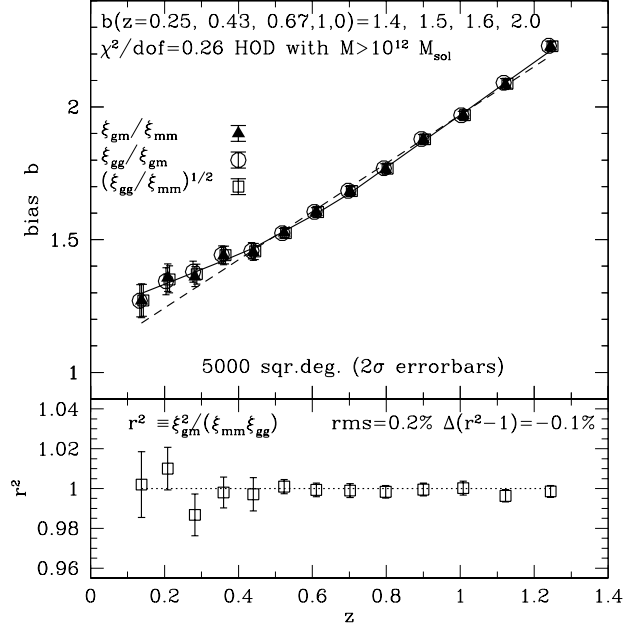


Figure 1. Bias in mock MICE galaxy simulations. Mean and (2-sigma) errors correspond to a 5000 deg² survey. Top panel shows the evolution of the effective bias defined in different ways: $\sqrt{\xi_{gg}/\xi_{mm}}$ (squares), ξ_{gg}/ξ_{gm} (circles) or ξ_{gm}/ξ_{mm} (triangles). The agreement is excellent: we include a small horizontal displacement to be able to see the different symbols. Continuous (or dashed) line shows the best fit bias evolution model: $b(z)$ based on linear inter/extrapolation from 4 (or 2) free bias parameters $b(z_i)$ spaced at regular scale factor values $a = 0.8, 0.7, 0.6, 0.5$ (or $a = 0.7, 0.5$). Bottom panel shows the cross-correlation coefficient $r^2 = \xi_{gm}^2 / (\xi_{gg}\xi_{mm})$.

2.4.2 Bias evolution

Figure 1 illustrates the above modeling as a function of redshift. Galaxy mocks are built from halos in the light-cone of a MICE simulation of side $L = 3072Mpc/h$ and $N = 2048^3$ particles (see Fosalba, Gaztanaga, Castander & Manera 2008, Crocce, Fosalba, Castander & Gaztanaga 2011 for more details on the simulation). The large size of this MICE run allows to build a light-cone sampling one octant of sky without repetition to $z = 1.5$. Halos are identified and weighted with a simple HOD (Halo Occupation Distribution) prescription. The number of galaxies in a halo of mass $M > M_{min}$ is $1 + (\frac{M}{20M_{min}})^\alpha$ with $M_{min} \simeq 10^{12} M_{sun}/h$ and $\alpha \simeq 1$ (e.g. see Scoccimarro et al. 2001).⁵ Evolution with redshift is all given by the halo mass evolution. We divide the light-cone simulation in redshift bins of width $\Delta z \simeq 0.1$ and estimate the correlations ξ_{mm} , ξ_{gm} and ξ_{gg} in each bin as a function of separation s . Three different bias parameters are then fitted to the ratios in Eq.18 on scales $s > 30Mpc/h$ where we find that these ratios are constant within the er-

⁵ This assignment can also introduce additional stochasticity but its contribution to ξ_ϵ vanishes if this stochasticity is not spatially correlated between halos

rors. Results for the different ratios agree well as shown in the top panel of Fig.1. These results indicates that $r \simeq 1$, as confirmed by the bottom panel. Errors are from a 100 jackknife angular patches which we have checked agree well with subsample errors (e.g. see Norberg et al. 2011 and references therein). The error-bars are similar for the different cases because sampling variance cancels to a good extend in the ratios. The bottom panel shows that r^2 is indeed very close to unity in agreement with the arguments above. The mean rms error in r is only 0.2% and the rms deviation from unity is less than -0.1% . Similar results are also found for different choices of HOD weights.

Note that because of the large volume and density of our simulation, the evolution of bias is known here to better than 1%. Halo model predictions do not yet reach these levels of accuracy (Manera, Shech & Scoccimarro 2010; Manera & Gaztañaga 2011), but could potentially be calibrated with simulations to achieve similar accuracies. As shown in the figure, the values at different redshift are strongly correlated, indicating that only a few parameters are needed to characterize the evolution of bias. The characteristic time scales for bias evolution in our samples seem to be $\Delta a > 0.1$, corresponding to $t > 1Gyr$, which is typical of galaxy evolution. This is also in agreement with recent bias measurements (e.g. Coupon et al 2011), which find a smooth dependence of observed bias with redshift for different galaxy luminosities and color, in good agreement with HOD. These results corresponds to $i_{AB} < 22.5$, similar to the sample that will be studied here. Systematics and selection effects do not seem to introduce higher frequency variations in the recovered biases.

Following these indications, we model $b(z)$ by including free bias parameters b_i at some fixed redshifts, with linear interpolation to other redshifts. We choose a constant spacing in scale factor $\Delta a_i = 0.1$ to fix the interpolation positions in $b(z)$. Given the redshift distribution of galaxies in our sample we choose 4 points as the interpolation locations: $a_i = 0.8, 0.7, 0.6, 0.5$, corresponding to redshift $z_i = 0.25, 0.43, 0.67, 1.0$. Fig.1 shows, as continuous line, a fit to such bias model. The fit has a χ^2 per degree of freedom of 0.26 which is “too good”. This indicates that this model has too many free parameters. If we use 2 bias parameters, instead of 4, at $a_i = 0.7, 0.5$, we find a χ^2 per degree of freedom of 1.2 (dashed line in the Figure). This indicates that 2 parameters is probably not enough, given the small error-bars. So 3 parameters seems to be the right number for large samples (5000 deg^2) and 2 parameters could be enough for smaller area surveys (ie 200 deg^2) which have larger errors. Here we will always use 4 parameters to be on the safe side.

In summary, we will use 4 biasing parameters with no priors as default, but also show how results change as a function of priors. Both from HOD modeling and from its comparison with observations we already have strong priors on what is the variation of bias for a given galaxy sample. These priors can also be estimated from the same data we are considering here. Recall that we will only be using linear scales in our forecast, while HOD modeling can take advantage of the data on smaller non-linear scales to constraint halo mass and HOD. Moreover, biasing could also be mea-

sured and constrained with other techniques, such as higher order correlations in the same galaxy sample (e.g. see Gaztanaga, Norberg, Baugh & Croton 2005, Sefusatti, Crocce, Pueblas & Scoccimarro 2006 and references therein).

2.5 Redshift Space distortions (RSD)

The measured redshift distance s to a galaxy differs from the cosmological distance r by its peculiar velocity \vec{v} along the line-of-sight. These displacements lead to redshift distortions. On large (linear) scales the dominant effect is due to coherent bulk motions induced by gravity. Mass conservation implies that the velocity divergence is $\theta \equiv \vec{\nabla} \cdot \vec{v} = -\dot{\delta}$, which on linear scales results in $\theta = -f\delta$ (see Eq.5). Thus in the line-of-sight direction fluctuations are distorted by a factor $(1 + f)$ resulting in a squashing effect in the 2-point redshift correlation function (Kaiser 1987). At small scales, random velocities inside clusters of galaxies produce a radial stretching pointing towards the observer, known as fingers of God (FOG). This have very little effect on linear scales considered here (Hikage, Takada & Spergel 2011).

The top left panel of Fig.2 shows the squashing effect in the amplitude of the 2-point correlation as a function of radial (vertical axes) and perpendicular (horizontal axis) separation (Gaztañaga, Cabré & Hui 2009). The squashing effect is quite clear in the inner regions of 20-50 Mpc/h and it also produces a large region with negative correlation between 50 and 100 Mpc/h which is characteristic of RSD (it is not present in the transverse direction). This effect allow us to measure f (Cabré & Gaztañaga 2009). One can also use this information to measure $H(z)$ from the BAO ring position at $\simeq 100 \text{ Mpc/h}$ (see Gaztanaga, Cabre & Hui 2009, Matsubara 2004) and put constraints on DE equation of state (Gaztanaga, Miquel & Sanchez 2010).

The remaining panels display the same measurements done over a distribution of objects with *photometric* redshifts of increasing photo-z error (as labeled). The distortion pattern due to coherent infall for the case of $\sigma_z = 0.003(1+z)$ (top right panel) is remarkably similar to the one in the original redshift sample. And it is precisely this anisotropic signal that we will employ to disentangle bias and growth of perturbations. For most purposes $\sigma_z \sim 0.003(1+z)$ is almost equivalent to having a (spectroscopic) redshift sample. This will be quantified better later. Notice how this agreement degrades rather quickly with σ_z .

In the large-scale linear regime and in the plane-parallel approximation (where galaxies are taken to be sufficiently faraway from the observer that the displacements induced by peculiar velocities are effectively parallel), the distortion caused by coherent infall velocities takes a particularly simple form in Fourier space (Kaiser 1987):

$$\delta_s(k, \mu) = (1 + f\mu^2)\delta(k) \tag{23}$$

where μ is the cosine of the angle between k and the line-of-sight, the subscript s indicates redshift space, and $f(z)$ is given by Eq. (5). If we assume that galaxy fluctuations are linearly biased by a factor b relative to the underlying matter density δ (i.e. $\delta_g = b\delta$) but velocities are unbiased,

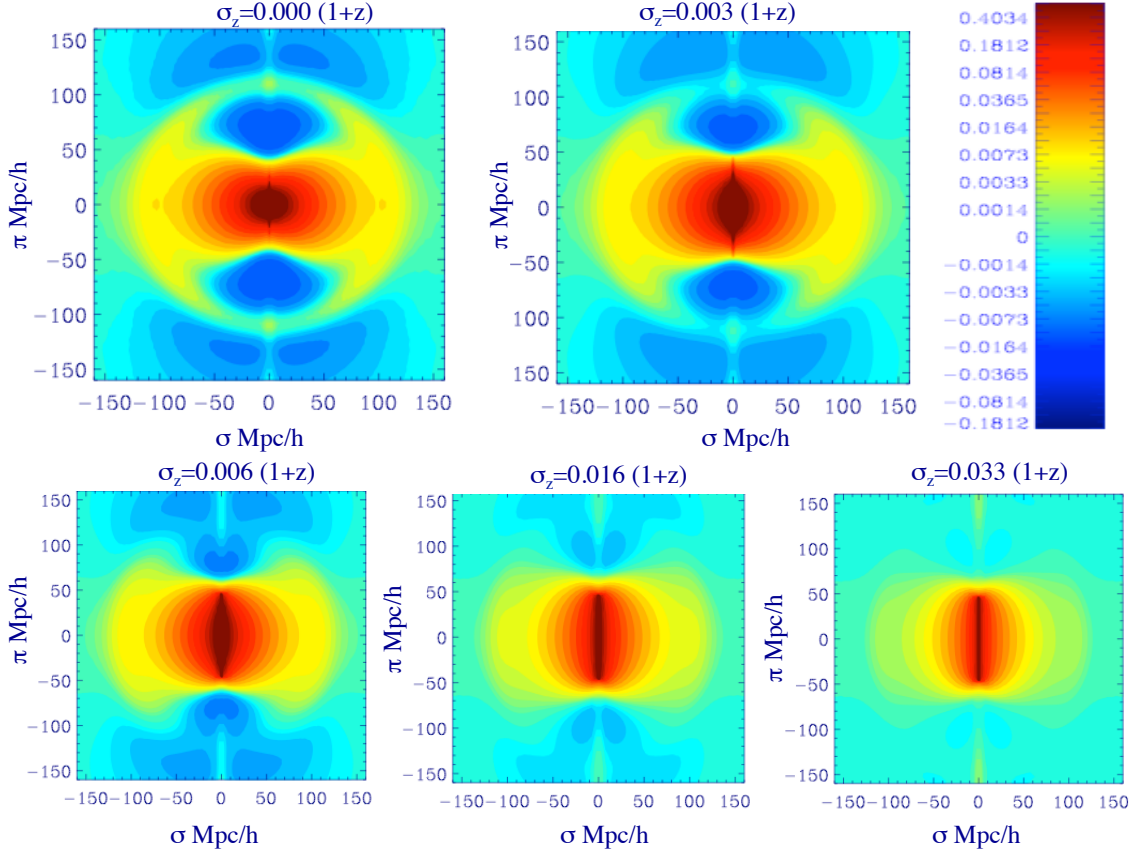


Figure 2. Top left panel shows the $\xi(\pi, \sigma)$ correlation in the Kaiser model with no photo- z error, i.e. $\sigma_z = 0$ (from Gaztañaga, Cabré & Hui 2009). The correlation is clearly squashed in the radial direction with a region of negative correlation (in blue) between $\pi = 50 - 100$ Mpc/h. Top right panel shows the same model but with a photo- z degradation of $\sigma_z = 0.003(1+z)$, corresponding to the PAU Survey. The difference is small and is mostly confined to small radial scales. Bottom panels show how the results are degraded as we increase σ_z to 0.006 (left), 0.016 (center) and 0.033 (right panel). As the photo- z increases the radial squashing disappears, turning instead into a radial elongation. Note also how the region of negative correlation vanishes as we increase the photo- z error.

then

$$\delta_g(k, \mu) = (b + f\mu^2)\delta(k) \quad (24)$$

where δ_g are the measured galaxy fluctuations in redshift space. However in practice what we measure is the rms value $\sigma(b + \mu^2 f)$, where σ is the r.m.s. amplitude of fluctuations at some scale. Hence by fitting the μ dependence we can have independent measurements of $b\sigma$ and $f\sigma$ as a function of redshift (or the ratio $\beta = f/b$, but we can not separate f from both σ or b). This means that $f(z)$ can not be measured unless we fix the normalization of $\delta(z)$. Combining RSD with weak lensing (see below) or higher order correlations in the same galaxy sample (e.g. see Gaztanaga, Norberg, Baugh & Croton 2005, Sefusatti, Crocce, Pueblas & Scoccimarro 2006 and references therein) we can break this degeneracy. Nonetheless having an estimate for $f(z)\sigma(z)$ (independent of bias) can be as valuable as just having f , as both are ways to constrain $D(z)$ and therefore γ .

To implement RSD constraints on the growth rate f and bias we follow the approach of White et al. (2009). First we write the cross power spectrum of galaxy samples A and B

at the same redshift bin i as,

$$P_{AB}^{(i)}(k, \mu) = (b_A + f\mu^2)(b_B + f\mu^2) G_{\sigma_z}(k, \mu) P_L(k) \quad (25)$$

where A and B are indices for different galaxy types and G_z

$$G_z(k, \mu) = \exp[-(1/2)k^2\mu^2(\sigma_A^2 + \sigma_B^2)] \quad (26)$$

accounts for the radial smearing due to photometric redshift uncertainties (and possibly the small scale peculiar velocity dispersion). The factor σ relates to the photo- z error σ_z by $\sigma = \sigma_z c/H(z)$. In Eq. (25) the bias b , the growth rate f and the photometric uncertainty σ are functions of redshift z_i . In turn, the linear power spectrum P_L is determined up to an overall normalization, say $\sigma_8(z) = D(z)\sigma_8(0)$, leading to the well known degeneracy between $f(z)$ or $b(z)$ and $\sigma_8(z)$. The FM corresponding to a given redshift bin i is (see Eq. (10)),

$$F_{\mu\nu}^i = \sum_{XY} \int \frac{V_0 d^3k}{(2\pi)^3} \left(\frac{\partial P_X^{(i)}}{\partial q_\mu} \right) C_{XY}^{-1} \left(\frac{\partial P_Y^{(i)}}{\partial q_\nu} \right) \quad (27)$$

where V_0 is the total volume of the redshift bin and $X, Y = (g_1g_1, g_1g_2, g_2g_2)$ in the case of two galaxy types or just $X = g_1$ for only one type. The derivatives in Eq. (27) for just one

population are simply given by,

$$\frac{\partial P}{\partial b} = \frac{2}{b + f\mu^2} P(k) \quad \text{and} \quad \frac{\partial P}{\partial f} = \frac{2\mu^2}{b + f\mu^2} P(k),$$

while the covariance matrix is,

$$\text{Cov}[P(k), P(k)] = 2P^2(k)N^2(k) \quad (28)$$

with $N(k) = 1 + (\bar{n}P(k))^{-1}$ and \bar{n} the galaxy number density. It is in this error term that the damping due to photometric uncertainty has an impact by increasing the shot-noise contribution to $N(k)$ and therefore the total error in $P(k)$. Expressions for the derivatives and covariance of two or more galaxy types can be readily obtained (see White et al. 2008).

The combination of parameters that are constrained with RSD are $q_\nu = b(z)\sigma_8(0)D(z)$ and $f(z)\sigma_8(0)D(z)$. In turn these depend on the set of cosmological parameters p_μ defined in Eq. (9) through Eqs. (1,5,6). To be able to join the constraints from RSD and WL we transform the variables by:

$$F_{p_\mu p_\nu} = M F_{q_\mu q_\nu} M^T \quad (29)$$

where $M = \partial p / \partial q$.

As explained in §2.2, the value of $\sigma_8(0)$ is dominated by priors so that we only measure relative amplitudes here. As we do not measure the shape of $P(k)$ either, in practice our forecast is equivalent to a measurement proportional to the ratio of the radial and transverse directions.

When we combine RSD with WL measurements we assume that these measurements are not correlated. This is not quite correct when the measurements are over the same area (FxB case below). To avoid the complication of estimating the full covariance of these two observables (i.e. $P(k)$ with C_ℓ) we will assume here that they are 100% correlated and make sure that we only count once the same modes (i.e. we use only independent measurements). This is a conservative approach as the true covariance will always be smaller. The total number of k -modes in the RSD case is:

$$dN_T(k) = \left(\frac{L}{2\pi}\right)^3 2\pi k^2 \mu dk d\mu \quad (30)$$

where L^3 is the volume of the survey region (e.g. within a redshift bin). This can be written as the product of purely transverse N_t and purely radial N_r modes:

$$\begin{aligned} dN_T(k) &= dN_t(k) dN_r(k) \\ dN_r(k) &= \left(\frac{L}{2\pi}\right) \mu kd\mu \\ dN_t(k) &= \left(\frac{L}{2\pi}\right)^2 2\pi k dk \quad (\mu = 0) \end{aligned} \quad (31)$$

In WL (or angular clustering) we will use the C_ℓ angular power spectrum which only measure purely transverse modes. This is easy to verify. If we use $k = \ell/\chi$ (where χ is radial distance and ℓ is the angular multipole) we find that $N_t(k) \simeq N(\ell) \simeq 4\ell$, as in the C_ℓ calculation in Eq.60). So we can avoid double counting by subtracting the purely

transverse modes from the RSD calculation:

$$N'_T(k) = N_T(k) - N_t(k) = N_T(k) \left(1 - \frac{1}{N_r(k)}\right) \quad (32)$$

where N'_T is the number of independent modes that can be used for RSD forecast when combined with WL (ie for the FxB case). This correction is small as $N_t(k) \gg 1$. In our case this can only affect the FxB combination and we have checked that this correction is always smaller than 30% in the final FoM.

3 WEAK LENSING

Weak lensing produces both a coherent distortion of galaxy shapes (known as shear distortion) and coherent magnification (MAG) of area that can be a source of density fluctuations. The latter is known as magnification bias or cosmic magnification (see e.g. Gunn 1967, Narayan 1989, Broadhurst et al. 1996 and references therein) which introduces both a correction to the angular galaxy auto correlation function (Villumsen, Freudling & da Costa 1997; Loverde, Hui & Gaztañaga 2008) and also to the cross-correlation of galaxies at different (including disjoint) redshifts (Moessner & Jain 1998; Hildebrandt et al. 2009). Magnification bias also changes the shape of the angular auto correlation function in RSD (Matsubara 2004; Hui, Gaztañaga, & Loverde 2007; Hui, Gaztañaga, & Loverde 2008), but these are relatively small effects, so we neglect them here from now on.

Measurements of cosmic magnification can provide comparable S/N to that of cosmic shear without the need to measure galaxy shapes (see e.g. Van Waerbeke 2009 and references therein). With spectroscopic or good photometric redshifts, such as those in PAU, one can further explore 3D lensing tomography by means of the angular cross correlation between galaxies in different narrow redshift bins, as will be explored here.

We follow the approach of Hu & Jain (2004 and references therein) who presented forecasts for shear and galaxy cross-correlations. As new ingredients, we will also consider the case for weak lensing MAG and the use of narrower redshift bins.

As we will show below, i.e. Eq.55 and Eq.58, both galaxy-galaxy and galaxy-shear cross-correlations of narrow redshift bins produce a direct measurement of the power spectrum of the foreground (lensing) distribution. This allows for a 3D reconstruction of the power spectrum, with a radial resolution that is much better than possible with the shear-shear reconstruction, i.e. Eq.57. The smaller the bin width, the better the reconstruction. In our forecast we are limited radially by the accuracy of the Limber approximation, which breaks for very narrow bins. To simply the analysis we also want to be able to neglect the intrinsic cross-correlations of separate bins. To achieve this, we find that we should use redshift bins which are larger than about $0.014(1+z)$ (i.e. > 60 Mpc/h) for which these approximations are adequate. Better results could in principle be obtained by using smaller bin widths, but this is left for a future analysis. In this sense our results are conservative.

3.1 Magnification & Shear

Magnification μ is defined as:

$$\mu = \frac{1}{\det A} = \frac{1}{(1 - \kappa)^2 - |\gamma|^2} \quad (33)$$

where A is the Jacobian matrix for the lensing transformation (see e.g. Bartelmann & Schneider 2000). In the weak lensing limit, fluctuations in magnification μ , convergence κ and shear γ are closely related. Fluctuations in (E-field) shear ϵ and convergence are equal, $\delta_\kappa = \delta_\epsilon$ (see e.g. Hu & Jain 2004) and, according to Eq.33, they are half as large as magnification $\delta_\mu = 2\delta_\kappa$. As κ can be obtained from shear measurements, we will also use κ to refer directly to shear. But we should bear in mind that some shear estimators are given in terms of $\delta\kappa/2$ (e.g. the iCosmos software of Refregier et al. 2011) and other combinations. In our FM approach this will only be relevant when introducing the scale for the intrinsic noise ellipticity.

We will focus here in convergence, δ_κ , as reconstructed from galaxy shapes measurements (that we will call shear), and magnification, δ_μ , as estimated from fluctuations in galaxy number density counts. Magnification changes the area of the background sources behind lenses, this induces a background fluctuation $\delta_g \simeq -\delta_\mu$ which is correlated with the foreground galaxy population. Additionally, background magnitudes are also affected inducing additional galaxy density fluctuations in δ_g across the sample magnitude limit. Adding both contributions gives

$$\delta_g = (2.5s - 1)\delta_\mu \simeq (5s - 2)\delta_\kappa \quad (34)$$

where s here is the slope of the galaxy number counts at the flux limit. Dust extinction in the lenses can also produce significant fluctuations. Menard et al. (2010) have shown that at sufficient large wavelengths, i.e. I and Z bands, dust extinction becomes negligible and the change in magnitude is dominated by magnification. In our analysis we will use I magnitudes to select galaxies and neglect dust extinction, although this might not always be a good approximation (see Fang et al. 2011).

Weak lensing convergence in bin j is given by the projected matter density δ_{m_i} in all foreground redshifts $i < j$:

$$\delta_{k_j}(\vec{\theta}) = \sum_{i < j} \bar{p}_{ij} \delta_{m_i}(\vec{\theta}) \quad (35)$$

where $\bar{p}_{ij} < 1$ is a geometrical WL weight that will be introduced later on and $\vec{\theta}$ are sky positions. We then have the following relation between observed galaxy fluctuation at background bin j , i.e. $\hat{\delta}_{g_j}$, and the foreground DM distribution:

$$\hat{\delta}_{g_j}(\vec{\theta}) \simeq b_j \delta_{m_j}(\vec{\theta}) + \epsilon_j(\vec{\theta}) + \sum_{i < j} p_{ij} \delta_{m_i}(\vec{\theta}) \quad (36)$$

where $p_{ij} = (5s - 2)\bar{p}_{ij}$ and we have used the linear local bias with stochasticity ϵ , defined in Eq.19. If we neglect ϵ we can use the observed $\hat{\delta}_g(\vec{\theta})$ and $\delta_k(\vec{\theta})$ maps and the above Eq.36 and Eq.35 to reconstruct both $\delta_m(\vec{\theta})$ and also b_i and p_{ij} (see Pen 2004). In general it is not clear to what extent we can neglect ϵ . What we do here instead is to

consider cross-correlations. The galaxy-galaxy and galaxy-shear cross-correlations then relates directly to the matter auto correlations

$$\begin{aligned} \langle \hat{\delta}_{g_i} \hat{\delta}_{g_i} \rangle &\simeq b_i^2 \langle \delta_{m_i} \delta_{m_i} \rangle \\ \langle \hat{\delta}_{g_i} \hat{\delta}_{g_j} \rangle &\simeq b_i p_{ij} \langle \delta_{m_i} \delta_{m_i} \rangle \quad i < j \\ \langle \hat{\delta}_{g_i} \hat{\delta}_{k_j} \rangle &\simeq b_i \bar{p}_{ij} \langle \delta_{m_i} \delta_{m_i} \rangle \quad i < j \end{aligned}$$

where we keep only leading order in $p_{ij} \ll 1$. We have neglected $\langle \epsilon_i \delta_i \rangle$ and $\langle \epsilon_i \epsilon_j \rangle$ terms, which seems to be a good approximation on large linear scales as we find that $r = 1$ (see discussion in §2.4).

Galaxy-galaxy cross-correlations from pairs of different redshift bins can be combined with the galaxy-galaxy auto-correlation to measure bias b_i and p_{ij} and $\langle \delta_{m_i} \delta_{m_i} \rangle$ with a radial precision given by the number of independent redshift bins. The same information can also be obtained from combining galaxy-shear cross-correlation and galaxy-galaxy autocorrelation.

Note that in our approach we ignore all the radial modes as the intrinsic $\langle \delta_{m_i} \delta_{m_j} \rangle$ correlation is negligible for disjointed top-hat bins $i \neq j$ when $\Delta z > 0.02$. It could be possible to include radial modes by using smaller redshift bins but this requires going beyond the Limber approximation, a study that we leave for future analysis (see Challinor & Lewis 2011). In this sense our results are conservative, as we do not include radial modes or very fine radial bins. As we increase the radial resolution (or number of independent redshift bins) the number of independent transverse modes $k_i = \ell/r_i$ also increases.

Finally, recall that we do not include redshift space distortions (RSD) in the modeling of angular correlations. This is a very good approximation for lensing because it has a very broad radial window which washes away the effect of radial peculiar velocities. For the angular galaxy-galaxy auto-correlation in narrow redshift bins, this is not a good approximation (see Nock et al. 2010, Crocce, Cabré & Gaztañaga 2010 and references therein). As mentioned in §2.3 our approach is to model angular clustering as transverse modes in real space and include the effect of RSD through the ratios of the amplitude of clustering as we change from transverse to radial modes within a single redshift bin (see §2.5).

3.2 Correlations & Power spectrum

Consider measurements of angular galaxy density and shear in a set of z -bins $i = 1, \dots, N_z$. Then the projected measurement of A in bin i is:

$$\delta_{A_i}(\vec{\theta}) = \int dz p_{A_i}(z) \delta_m(r\vec{\theta}, z) \quad (37)$$

where δ_m is the 3D dark matter fluctuation, $\vec{\theta}$ gives the angular position, $r = r(z)$ is the comoving transverse (or angular diameter) distance to redshift z and p_{A_i} is the radial weight defined later. The label A refers to either the galaxy fluctuation, i.e. $A = g$, or a shear measurement of convergence, i.e. $A = \kappa$.

The observables to measure are the galaxy-galaxy (gg), galaxy-shear ($g\kappa$) and shear-shear ($\kappa\kappa$) cross-correlations of

angular fluctuations between redshift bins i and j , which are denoted by:

$$w_{g_i g_j}(\theta) \equiv \langle \delta_{g_i}(\vec{\theta}_1) \delta_{g_j}(\vec{\theta}_2) \rangle \quad (38)$$

$$w_{\kappa_i \kappa_j}(\theta) \equiv \langle \delta_{\kappa_i}(\vec{\theta}_1) \delta_{\kappa_j}(\vec{\theta}_2) \rangle \quad (39)$$

$$w_{\kappa_i g_j}(\theta) \equiv \langle \delta_{\kappa_i}(\vec{\theta}_1) \delta_{g_j}(\vec{\theta}_2) \rangle \quad (40)$$

where $\theta = |\vec{\theta}_2 - \vec{\theta}_1|$ is the angular separation between 2 measured fluctuations of galaxy density δ_g or galaxy shear δ_κ (see Bernstein 2009 for generalizations of this). It is convenient to express $w(\theta)$ in terms of harmonic coefficients $C(\ell)$:

$$w(\theta) = \sum_{\ell} \frac{2\ell + 1}{4\pi} C(\ell) L_{\ell}(\cos \theta) \quad (41)$$

$$C(\ell) \equiv 2\pi \int_{-1}^1 d \cos \theta w(\theta) L_{\ell}(\cos \theta) \quad (42)$$

where $L_{\ell}(\cos \theta)$ are Legendre polynomials of order ℓ . Thus we have galaxy-galaxy, $C_{g_i g_j}(\ell)$, shear-shear, $C_{\kappa_i \kappa_j}(\ell)$ and galaxy-shear, $C_{g_i \kappa_j}(\ell)$ cross power spectrum between bin i and j . Our galaxy sample is split into different galaxy types (or populations) that we label by gn , where n can take N_t values (we only use $N_t = 2$ here, but this can be easily extended), ie $n = 1, 2, \dots, N_t$, for each population with different bias. We do not split shear by populations because we assume that shear is independent of bias. Thus the total number of observables for 2 populations, $N_t = 2$, is then:

$$C_{ij}(\ell) \equiv [C_{g1_i g1_j}(\ell), C_{g2_i g2_j}(\ell), C_{g1_i g2_j}(\ell), C_{g1_i \kappa_j}(\ell), C_{g2_i \kappa_j}(\ell), C_{\kappa_i \kappa_j}(\ell)] \quad (43)$$

For a generic cross-correlation we will use the notation:

$$C_{A_i B_j}(\ell) \quad (44)$$

where A and B can take the values κ for shear or $g1, g2, \dots, gN_t$ for different galaxy types. Note that while $C_{A_i A_j} = C_{A_j A_i}$, in general:

$$C_{A_i B_j}(\ell) = C_{B_j A_i}(\ell) \quad (45)$$

$$C_{A_i B_j}(\ell) \neq C_{A_j B_i}(\ell) \text{ for } A \neq B; i \neq j \quad (46)$$

In the small angle approximation (Limber 1954, Loverde & Afshordi 2008), there is a simple relation between $C(\ell)$ and the 3D matter power spectrum $P(k) \equiv \langle \delta^2(k) \rangle$:

$$C_{A_i B_j}(\ell) = \int_0^{\infty} dz p_{A_i}(z) p_{B_j}(z) \mathcal{P}(k, z) \quad (47)$$

$$\mathcal{P}(k, z) \equiv \frac{P(k, z)}{r_H(z) r^2(z)} \quad (48)$$

where $r_H(z) \equiv c/H(z)$, and \mathcal{P} is the a -dimensional power spectrum at $k = (\ell + 1/2)/r$. In linear theory $P(k, z) = D^2(z)P(k)$.

3.3 Lensing weights

For shear or convergence fluctuations, i.e. $A = \kappa$ the redshift distribution $p_A = p_\kappa$ in the above equation corresponds to the weak lensing efficiency between sources in redshift bin j

and dark matter (lenses) at z :

$$p_{\kappa_j}(z) \equiv \frac{3\Omega_m H_0 r(z)}{2H(z)a(z)r_0} \int_z^{\infty} dz' \frac{r(z'; z)}{r(z')} \phi(z') \quad (49)$$

where Ω_m is the DM density at $z = 0$, $r_0 = c/H_0$, $a(z) = 1/(1+z)$. Here $r(z'; z)$ is the angular diameter distance between z' and z and $\phi_j(z)$ is the normalized galaxy probability density distribution for source galaxies in the redshift bin label j . For a uniform galaxy distribution in a top-hat window of total width Δ_j :

$$\phi_j(z) = \begin{cases} 1/\Delta_j & \text{for } |z - z_j| < \Delta_j/2 \\ 0 & \text{otherwise.} \end{cases} \quad (50)$$

3.3.1 Narrow bin approximation

For narrow redshift bins we approximate p_κ in Eq.49 by:

$$p_{ij} \equiv p_{\kappa_j}(z_i) \simeq \frac{3\Omega_m H_0}{2H(z_i)a_i} \frac{r_i r(z_j; z_i)}{r_0 r_j} \text{ for } i < j \quad (51)$$

where $r_i \equiv r(z_i)$. This is an excellent approximation for the non-overlapping top-hat bins in our problem. For example for sources at $z_i = 1$, and a bin width of $\Delta z_i = 0.1$ (which is 30 times larger than our default value at $z_i = 1$) the accuracy of this approximation is better than 0.7% for $z < 0.95$, which is all we need for non-overlapping z bins. This is illustrated in Fig.3, which compares the exact calculation (squares) with the approximation (lines across the squares) for $\Delta z_i = 0.05$. This approximation greatly simplifies Eq.47, which becomes a single integral that can be done analytically for the galaxy-galaxy and the galaxy-shear case. Also note that p_κ in this approximation is independent of the redshift bin width.

3.4 Galaxy weight

For galaxy type “ n ”, i.e. $A = gn$, the redshift distribution $p_A = p_{gn}$ in the Eq.47, corresponds to the sum of the intrinsic number density and the lensing magnification contribution (see Eq.36):

$$p_{gn_i}(z) = b_{n_i} \phi_{n_i}(z) + \alpha_{n_i} p_{\kappa_i}(z) \quad (52)$$

where $b_{n_i} \equiv b_n(z_i)$ is the mean linear galaxy bias for galaxy type n at redshift bin i . The second term is due to weak lensing magnification with

$$\alpha_{n_i} \equiv \alpha_n(z_i) \equiv 5s_n(z_i) - 2 \quad (53)$$

where $s_n(z_i)$ is the slope of the number counts $N_n(< m; z_i)$ of galaxies of type n with apparent magnitude smaller than the survey flux limit m (plus whatever other cuts we do to the survey) at $z = z_i$

$$s_n(z_i) \equiv \frac{d \log_{10} N_n(< m; z_i)}{dm} \quad (54)$$

Its value can be estimated using the same galaxy sample. We then have that α_n modulates the weak lensing magnification effect of dark matter fluctuations at $z < z_i$. It is clear from this that both shear and magnification could measure the

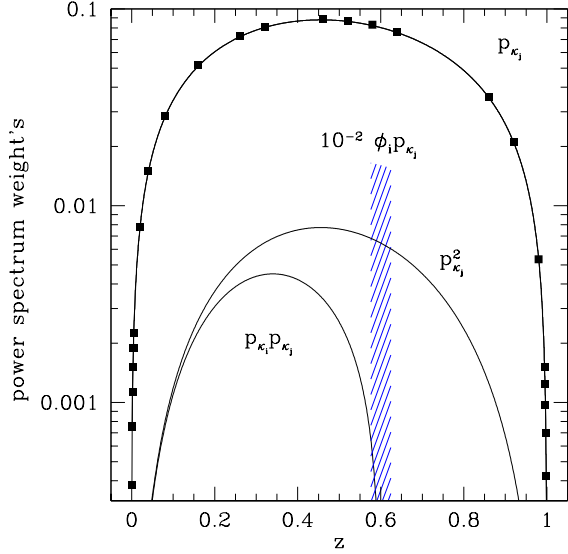


Figure 3. Filled squares show the weak lensing efficiency $p_{\kappa_j}(z)$ in Eq.49 as a function of the lensed position z for a source at $z_j = 1.0$. The line across the squares corresponds to the approximation in Eq.51. The other two lines show the weights $p_{\kappa_j}^2$ and $p_{\kappa_i} p_{\kappa_j}$ applied to the matter power spectrum $\mathcal{P}(k, z)$ in the shear-shear auto and cross-correlation of Eq.57 for $z_i = 0.6$. These distributions are always very broad, indicating that shear-shear can only measure the projected (2D) power. The shaded region shows the corresponding weights for galaxy-galaxy cross-correlation from MAG (or galaxy-shear), ie $\phi_{z_i} p_{\kappa_j}$, for $\Delta_i = 0.05$. Here the power spectrum is measured in 3D with a resolution that is only limited by Δ_i .

same information, modulo α_n , noise and systematics, but in practice we need to study their correlations, which we do next.

3.5 Galaxy-Galaxy (Magnification)

For narrow and disjoint redshift bins we have from Eq.47 that for $i \leq j$,

$$C_{g_{n_i} g_{m_j}}(\ell) \simeq \left[b_{n_i} b_{m_i} \frac{\delta_{ij}}{\Delta_i} + \alpha_{m_j} b_{n_i} p_{ij} \right] \mathcal{P}_i + \alpha_{n_i} \alpha_{m_j} C_{\kappa_i \kappa_j}(\ell) \quad (55)$$

where δ_{ij} is the Kronecker delta and $\mathcal{P}_i \equiv \mathcal{P}(k_i, z_i)$ in Eq.48, with $k_i = (\ell + 1/2)/r(z_i)$. When $i = j$ the first term dominates (as $p_{ii} = 0$), while for $i \neq j$ the second term is dominant (as $\delta_{ij} = 0$). The last term is always sub-dominant and will be neglected here.⁶ So we see here how galaxy cross-correlations can be used to measure 3D power spectrum without the need of shear measurements.

The nuisance biases b_{n_i} , can be measured by comparing C_{ij} with C_{ii} . The main source of contamination here

⁶ But note that if we can measure very well the two first terms, the last term contains all the shear-shear information, without need of direct shear measurements.

is intrinsic or induced correlations of galaxies in bin i with the ones in bin j . If these bins are well separated this can only occur because of photo- z transitions, ie galaxies moving from one redshift bin to another due to photo- z errors (see §3.11 and §3.12 for details).

The different pair combinations can be used to simultaneously measure b_i , \mathcal{P}_i and p_{ij} . To illustrate this claim, consider the ratio: C_{ij}/C_{ik} when $i \neq j \neq k$ we have:

$$\frac{C_{ij}(\ell)}{C_{ik}(\ell)} = \frac{\alpha_j p_{ij}}{\alpha_k p_{ik}} \quad (56)$$

which are independent of bias and the power spectrum for any value of ℓ . This is also true in the non-linear regime (i.e. with non-linear bias and non-linear dark matter clustering). This is therefore a direct geometrical measure. In a similar way one can build up ratios like C_{ii}/C_{ij} to measure b_i independent of \mathcal{P}_i , or C_{ij}^2/C_{ii} to measure \mathcal{P}_i with independence of bias b_i .

3.6 Shear-Shear

For the shear-shear term with $i < j$ the cross-correlations are:

$$C_{\kappa_i \kappa_j}(\ell) = \int_0^{z_j} dz p_{\kappa_i}(z) p_{\kappa_j}(z) \mathcal{P}(k, z) \quad (57)$$

$$\simeq \int_0^{z_i} dz \frac{dz}{r_H} \left(\frac{3\Omega_m H_0}{2H_{ar0}} \right)^2 \frac{r(z_i; z) r(z_j; z)}{r_i r_j} \mathcal{P}(k, z)$$

and $C_{\kappa_i \kappa_j} = C_{\kappa_j \kappa_i}$ for $j < i$. It is also possible to combine here different pairs of bins to get some tomographic (3D) information, but as illustrated in Fig.3 the resulting weights are very broad, even if we use narrow galaxy bins. This means that the tomographic recovery is quite limited.

3.7 Galaxy-Shear

Finally, for narrow bins, we also find the galaxy-shear cross-correlation from Eq.47 for $i < j$:

$$C_{g_{n_i} \kappa_j} \simeq b_{n_i} p_{ij} \mathcal{P}_i + \alpha_{n_i} C_{\kappa_i \kappa_j} \quad (58)$$

and $C_{\kappa_i g_{n_j}} = 0$ for $i < j$. Thus the off-diagonal information content of $C_{g_{n_i} \kappa_j}$ is identical (except for the global factor α_{m_i}) to that of $C_{g_{n_i} g_{m_j}}$, even when the noise and the systematic could be quite different.

3.8 3D $\mathcal{P}(k)$ recovery

A comparison of Eq.58 or Eq.55 with Eq.57 illustrates how cross-correlations of galaxy-galaxy or galaxy-shear both recover the full 3D power spectrum, i.e. $\mathcal{P}(k)$, while the shear-shear only provides an integral over very broad redshift distribution. This is illustrated in Fig.3, which shows that $p_{\kappa_i} p_{\kappa_j}$ in Eq.57 is always very broad, while $\phi_{z_i} p_{\kappa_j}$ can be as narrow as needed.

Another point to note is the fact that the galaxy-galaxy or galaxy-shear cross-correlations only depend on $p_k \simeq 10^{-1}$ while shear-shear depends on $p_k^2 \simeq 10^{-2}$. This means that

the amplitude of shear-shear correlation is much smaller and is therefore sensitive to smaller amplitudes in systematic effects. Moreover, the effect of systematics will tend to cancel in a cross-correlation analysis to a larger extent than in the auto-correlation. But these are generic considerations and ultimately the key point is that systematics are quite different in both measurements.

3.9 Covariance

In the Gaussian limit, the covariance between one pair of observables in Eq.43 at redshift bins (ij) and another pair at redshift bins (kl) is given by:

$$\Theta_{ij;kl} \equiv \text{Cov}(C_{ij}; C_{kl}) = \frac{\hat{C}_{ik}\hat{C}_{jl} + \hat{C}_{il}\hat{C}_{jk}}{N(\ell)} \quad (59)$$

where $N(\ell)$ is the number of modes at a given ℓ . In our case we bin the l modes as $\Delta\ell \simeq 2/f_{sky}$ (see Cabre et al. 2007) to avoid correlation induced by the limited fraction of sky covered (f_{sky}). The number of modes of each ℓ is then

$$N(\ell) = (2\ell + 1)f_{sky}\Delta\ell \simeq 2(2\ell + 1) \quad (60)$$

The observables \hat{C} in the covariance include observational noise:

$$\hat{C}_{gn_i gm_j} = C_{gn_i gm_j} + \frac{1}{\bar{n}_{gn}} \delta_{ij} \delta_{nm} \quad (61)$$

$$\hat{C}_{\kappa_i \kappa_j} = C_{\kappa_i \kappa_j} + \frac{\sigma_\kappa^2}{\bar{n}_\kappa} \delta_{ij} \quad (62)$$

$$\hat{C}_{\kappa_i gn_j} = C_{\kappa_i gn_j} \quad (63)$$

where \bar{n}_κ and \bar{n}_{gn} are the surface density of galaxies with measured shear and galaxies of type n with good photometry respectively and σ_κ^2 is the variance in convergence from intrinsic ellipticities. Note that $\sigma_\kappa < 1$ while $\bar{n}_{gn} > \bar{n}_\kappa$ so that the noise could be larger or smaller in shear-shear than in galaxy-galaxy, depending on the depth and quality of data.

3.10 Signal to Noise

From the above covariance we can estimate the signal to noise S/N ratio for the galaxy auto-correlation $C_{g_i g_i}(\ell)$

$$(S/N)_{g_i g_i}^2 = \frac{N(\ell)}{2} \quad (64)$$

and compare it to the galaxy-galaxy cross-correlation $C_{g_i g_j}(\ell)$

$$(S/N)_{g_i g_j}^2 \simeq \frac{C_{ij}^2 N(\ell)}{C_{ii} C_{jj}} \propto N(\ell) \Delta_i \Delta_j \propto \frac{N(\ell)}{N_z^2} \quad (65)$$

where in the first step we have used that $C_{ij}^2 < C_{jj} C_{ii}$ and $C_{ii} \propto 1/\Delta_i$, where $\Delta_i \propto 1/N_z$ is the redshift bin width and N_z is the number of redshift bins. The total S/N is the sum over all the N_z redshift bins. In the case of the cross-correlation there are $N_z(N_z - 1)/2$ pairs and therefore the total S/N is independent of the number of bins for large N_z . Something similar happens when considering RSD or in general 3D $P(k)$ measurements. This means that there is no S/N gain in using many redshift bins. We could gain information in cases where the signal varies on radial scales

comparable to the redshift bin width. Both cosmological parameters and galaxy formation (i.e. biasing) vary on scales $\Delta a = 0.1$. This means that there is no information gain in using smaller bins in this case.

In the case of galaxy-shear:

$$(S/N)_{g_i \kappa_j}^2 \simeq \frac{C_{g_i g_j}^2 N(\ell)}{C_{g_i g_i} C_{\kappa_j \kappa_j}} \propto N(\ell) \Delta_i \propto \frac{N(\ell)}{N_z} \quad (66)$$

Here there are only N_z galaxy-shear pairs per shear bin, so again the total signal to noise is quite insensitive to the number of bins.

In the case of the autocorrelation C_{ii} in Eq.64, the total S/N increases with number of bins and there is a net S/N gain in using more bins. This gain is only limited by the increase of shot-noise for small redshift bins and the fact that very narrow nearby bins are no longer independent. Thus, while shear-shear and galaxy-shear are useful to recover galaxy bias, the gain from using narrow bins comes from galaxy-galaxy auto correlations. This is a key point to understand the results in this paper.

3.11 Photo-z error transitions

First we study the case of galaxy-galaxy cross-correlations. Consider the transition probability T_{ij} that a galaxy at bin j is measured to be at bin i because of the photo-z error. The number of galaxies measured in bin i , \bar{N}_i , is then:

$$\bar{N}_i = \sum_j T_{ij} N_j \quad (67)$$

where N_j is the true number of galaxies in bin j . To include the effect of photo-z errors in the cross-correlations we need to define the relative transition probability, or migration matrix r_{ij} , as the fraction of the galaxies assigned to z-bin i which really are in bin j , ie:

$$r_{ij} \equiv T_{ij} \frac{N_j}{\bar{N}_i} = \frac{T_{ij} N_j}{\sum_j T_{ij} N_j} = \frac{T_{ij} \langle N_j \rangle}{\sum_j T_{ij} \langle N_j \rangle} \quad (68)$$

where by construction:

$$\sum_j r_{ij} = 1 \quad \forall i \quad (69)$$

Note that when r_{ij} is a smooth function of the redshift distance $z_j - z_i$, r_{ij} will also be independent of the redshift width Δz for $|z_j - z_i| > \Delta z$. These r_{ij} transitions correspond to the contamination matrix C_{ps} in Bernstein & Huterer (2010) and give the probability $P(z_s|z_p)$ for a true redshift is z_s to be measured in photo-z redshift z_p . The last equality in Eq.68 just indicates that the same probabilities apply for the mean density as for regions with fluctuations: $N_i \equiv \langle N_i \rangle (1 + \delta_i)$. We then have that the correlation $\bar{w}_{ij} \equiv \langle \bar{\delta}_i \bar{\delta}_j \rangle$ in photo-z space can be related to the true correlation $w_{ij} \equiv \langle \delta_i \delta_j \rangle$ as (see also Benjamin et al. 2010)

$$\begin{aligned} \bar{w}_{ij} &= \langle (1 + \bar{\delta}_i)(1 + \bar{\delta}_j) \rangle - 1 = \frac{\langle \bar{N}_i \bar{N}_j \rangle}{\langle \bar{N}_i \rangle \langle \bar{N}_j \rangle} - 1 \\ &= \sum_{kl} r_{ik} r_{jl} (1 + w_{kl}) - 1 = \sum_{kl} r_{ik} r_{jl} w_{kl} \quad (70) \end{aligned}$$

Thus, photo-z errors result in a mixing of the cross-correlation measurements:

$$\bar{C}_{ij} = \sum_{kl} r_{ik} r_{jl} C_{kl} \quad (71)$$

where \bar{C}_{ij} is the observed cross-correlation in photo-z space and C_{kl} is the true cross-correlation. The new covariance matrix (i.e. Eq.59) will now be:

$$\bar{\Theta} = \text{Cov}(\bar{C}; \bar{C}) \quad (72)$$

Note that noise (e.g. shot-noise) should be added to the observed (not the true) covariance. This could degrade the cosmological parameters correspondingly. These considerations can be extended trivially to the case of the cross-correlation of 2 galaxy populations. We will then have different transitions r_{ij} for each population and assume no transition between populations. In matrix notation:

$$\bar{C}_{g_1 g_2} = r_{g_1} C_{g_1 g_2} r_{g_2}^T \quad (73)$$

where r_{g_1} and r_{g_2} represent the transition matrix for galaxy populations g_1 and g_2 and T stands for the transpose matrix. In our case g_1 and g_2 can take the values of Faint, g_F , or Bright, g_B , galaxies.

For galaxy-shear and for shear-shear we use the same relations Eq.71-72 to account for photo-z contamination. In the case of shear, the observable is given by some mean over the number of galaxies where shapes are measured. So photo-z leakage has a different effect in shear fluctuations than in galaxy counts (see Bernstein & Huterer 2010). Nevertheless we note the shear correlations are also built from pairs of measurements and one can use the same relations as for galaxy-galaxy to account for photo-z contamination.

Consider a photo-z distribution $P(z_p|z)$ giving the probability that a galaxy at true redshift z is measured to be at z_p . For top-hat bins of width Δ_i and Δ_j we have:

$$T_{ij} = \int_{\Delta_j} \frac{dz}{\Delta_j} \int_{\Delta_i} dz_p P(z_p|z) \simeq \int_{\Delta_i} dz_p P(z_p|z_j) \quad (74)$$

where the integrals are around the corresponding top-hat bins centered in z_i and z_j . In the second equality above we have approximated the integral over bin j' by its mean value. Note that $T_{ij} \neq T_{ji}$ because the distribution $P(z|z_p)$ is in general different for different z (i.e. typically photo-z errors are a function of z). For a Gaussian photo-z distribution with error $\sigma_z = \sigma_z(z_j)$

$$\begin{aligned} T_{ij} &= \int_{z_{ij}-\Delta_j/2}^{z_{ij}+\Delta_j/2} \frac{dx}{2\Delta_j} \left[\text{erf}\left(\frac{2x+\Delta_i}{\sigma_z\sqrt{8}}\right) - \text{erf}\left(\frac{2x-\Delta_i}{\sigma_z\sqrt{8}}\right) \right] \\ &\simeq \frac{1}{2} \left[\text{erf}\left(\frac{2z_{ij}+\Delta_i}{\sigma_z\sqrt{8}}\right) - \text{erf}\left(\frac{2z_{ij}-\Delta_i}{\sigma_z\sqrt{8}}\right) \right] \end{aligned} \quad (75)$$

where $z_{ij} \equiv z_j - z_i$, and $\text{erf}(x)$ is the standard error function (integration of a normal from 0 to x).

In general, it is possible to recover r_{ij} from the observables given some model for the intrinsic correlations, even without the combination of spectroscopic and photometric samples. The cross-correlation of spectroscopic and photometric samples provides another route to measure r_{ij} , extending the proposal by Newman (2008) to the cross-correlation in separate redshift bins.

3.12 Uncertainties in the Photo-z transitions

So far we have seen how it is possible to correct for photo-z errors. Here we will quantify how the uncertainties in our knowledge of the photo-z transitions r_{ij} , which we will denote by Δ_{ij} , could affect our predictions. From Eq.71 we find that the error in \bar{C}_{ij} is:

$$\Delta \bar{C}_{ij} = \sum_{\alpha} (R_{\alpha j} \Delta_{i\alpha} + L_{i\alpha} \Delta_{j\alpha}) \quad (76)$$

where we have defined the matrices R and L as:

$$L_{ij} \equiv \sum_k r_{ik} C_{kj} \quad ; \quad R_{ij} \equiv \sum_k r_{jk} C_{ik} \quad (77)$$

For a spectroscopic sample in the foreground (background) we have that $L \simeq C$ ($R \simeq C$). We will assume that this uncertainty is the same $\Delta_r = \Delta_{ij}$ for all pairs ij and that they are uncorrelated, so

$$\langle \Delta_{ij} \Delta_{kl} \rangle = \delta_{ik} \delta_{jl} \Delta_r^2 \quad (78)$$

where δ_{ik} and δ_{jm} are the Kronecker deltas. Note that in a more realistic situation errors could be different for different transitions, i.e. $\langle \Delta_{ij}^2 \rangle \neq \langle \Delta_{kl}^2 \rangle$, but here we just want to evaluate the overall size of this effect. One can easily extend this analysis to a more generic situation. The covariance caused by this uncertainty is then:

$$\begin{aligned} \Theta_{ij;kl} &\equiv \text{Cov}[\bar{C}_{ij}; \bar{C}_{kl}] = \langle \Delta \bar{C}_{ij} \Delta \bar{C}_{kl} \rangle = \Delta_r^2 \\ &\times [\delta_{ik} (R^T R)_{jl} + \delta_{il} (L R)_{kj} + \delta_{jk} (L R)_{il} + \delta_{jl} (L L^T)_{ik}] \end{aligned} \quad (79)$$

Note that \bar{C}_{ij} here does not include shot-noise as we are evaluating the uncertainty in the \bar{C}_{ij} prediction, for a given value and error in r_{ij} . This covariance is then added to the covariance matrix in Eq.72, that includes the observational noise, to explore how the FoM degrades as a function of the uncertainties in the bin transition Δ_r . This will give us an idea of how well we need to know r_{ij} for a given required FoM value.

When we have different populations or cross-correlation of different observables (ie, galaxy with shear) we can easily generalize the above expressions, e.g.:

$$\Delta \bar{C}_{A_i B_j} = \sum_{\alpha} \left(R_{A_{\alpha} B_j} \Delta_{i\alpha}^A + L_{A_i B_{\alpha}} \Delta_{j\alpha}^B \right) \quad (80)$$

where Δ^A is the uncertainty for type A . Types A and B can refer to density fluctuations (e.g. $A = g_F$ or $A = g_B$ for Faint and Bright) and the same formalism can also be applied to shear.

4 FIDUCIAL GALAXY SURVEYS

We compare results for combinations of two galaxy samples: a deep ($i_{AB} < 24$) sample, that we call Faint (F), and a shallower ($i_{AB} < 22.5$) sample, call Bright (B). We consider four cases: the two samples alone and two ways to combine them. In one of the combinations (call F+B) we assume that the two samples are independent, ie over different parts of the sky. In the other combination (call FxB) we assume that they are over the same region of sky: typically one can think the B sample as a spectroscopic follow-up of the F sample.

4.1 Faint Sample (F)

The F sample is a photometric survey with a broad band photo-z error:

$$22.5 < i_{AB} < 24 \quad \text{and} \quad \sigma_z \simeq 0.05(1+z)$$

similar to the upcoming DES (Dark Energy Survey, www.darkenergysurvey.org). We assume that we have very good photometry to be able to measure magnification and also shear (galaxy shape) information. But we will show results for magnification alone, shear alone and both combined.

The cut at the bright end, $i_{AB} > 22.5$ is not an essential ingredient. It is included to make this sample separate in magnitude from the B sample, but all the results to follow are almost identical without such a cut. This selection results in:

$$\frac{dN}{d\Omega dz} = 7.342 \times 10^4 (z/0.467)^{1.913} e^{-(z/0.467)^{1.274}} \quad (81)$$

over $0.1 \lesssim z \lesssim 2.0$, where $dN/d\Omega dz$ is in units of number of galaxies per deg^2 . This is a fit to an evolving luminosity function that matches Blanton et al. (2003), Dahlen et al. (2005, 2007) and Jovel et al. (2009). The above redshift distribution includes a completeness reduction of $\sim 50\%$. For a survey of 200 deg^2 it yields $\sim 6 \times 10^6$ galaxies. Note that we often refer to this sample briefly as $i_{AB} < 24$, but we always use a lower cut $i_{AB} > 22.5$, so that galaxies are clearly separated from the Bright sample. This avoids potential photo-z transitions between the two samples. The upper line in Fig.4 illustrates the above model and compares it with the actual data in the public COSMOS photo-z sample (Ilbert et al., 2010) which has about 100000 galaxies over 2 deg^2 area with $22.5 < i_{AB} < 24$ and mean photo-z redshift of $\bar{z} = 0.9$ for $z > 0.2$. Note that this area is quite small and subject to large sampling fluctuations (see Fosalba et al. 2007).

For the fiducial bias in this sample we use four bias parameters b_i^F at $z_i = 0.25, 0.43, 0.67$ and 1.0 with linear interpolation to other redshifts (see §2.4). The fiducial values for the 4 bias parameters follow:

$$b_i^F = 1.2 + 0.4(z_i - 0.5),$$

so that the bias approaches unity at $z = 0$ and has a linear scaling, as shown in Fig.1. We then allow the 4 bias parameters to vary without priors around these fiducial values.

Note that we only consider WL and angular galaxy clustering probes for the Faint sample alone. It is also possible to measure RSD here even with poor photo-z (e.g. see Nock et al. 2010, Crocce, Cabré & Gaztañaga 2010, Ross et al 2011, Crocce et al. 2011) but we have checked that the additional FoM is small compared to the one in spectroscopic surveys and decided to restrict to the more traditional use of photometric surveys.

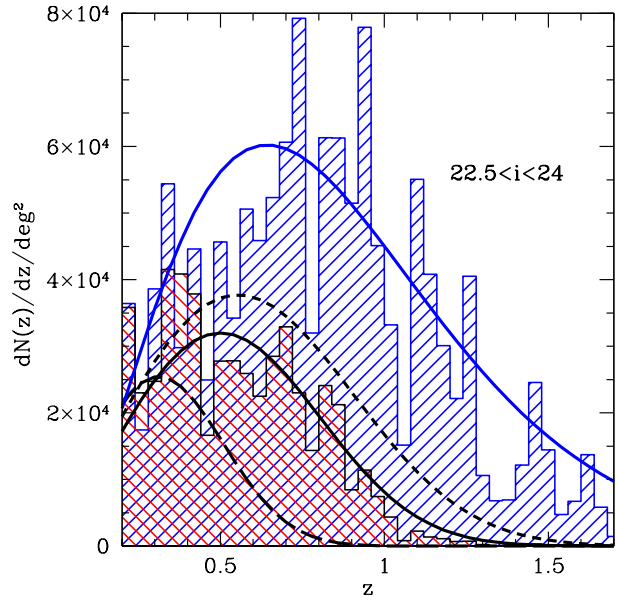


Figure 4. Upper and lower continuous lines show the number of galaxies per deg^2 in our complete fiducial F (faint) sample with $22.5 < i_{AB} < 24$ and the B (bright) sample with $i_{AB} < 22.5$ i.e. Eq.81 and Eq.82 multiplied by 2 to make then complete. Histograms show the actual measurements in the COSMOS photo-z survey which has $\bar{z} = 0.90$ and $\bar{z} = 0.57$ respectively for $z > 0.2$. The long and the short dashed lines show the corresponding fits to $i_{AB} < 21.5$ and $i_{AB} < 23.0$.

4.2 Bright Sample (B)

The bright sample is a spectroscopic sample or very good photo-z without lensing information and defined by a flux limit:

$$i_{AB} < 22.5$$

which results in:

$$\frac{dN}{d\Omega dz} = 3.481 \times 10^4 (z/0.702)^{1.083} e^{-(z/0.702)^{2.628}} \quad (82)$$

over $0.2 \lesssim z \lesssim 1.25$ also including a completeness of 50% , as in the faint sample. For a survey of 200 deg^2 it yields $\sim 2 \times 10^6$ galaxies. The lower solid line in Fig.4 illustrates the above model and compares it with the actual data in the public COSMOS photo-z sample (Ilbert et al., 2010) which has about 43000 galaxies with $i_{AB} < 22.5$ with a mean photo-z redshift of $\bar{z} = 0.57$ for $z > 0.2$.

The fiducial photo-z errors will be $\sigma_z \simeq 0.0035(1+z)$, based on the PAU concept of using narrow band filters (see §1). On linear scales, larger than 20 Mpc/h , this is almost equivalent to spectroscopic accuracy. In §5.8 we will explore the dependence of the results with photo-z error. Later on, in §6, we will also consider a sample named “Bspec” with spectroscopic redshifts ($\sigma_z = 0$) but with a lower density of

1000 galaxy/deg². Dependence on density will be considered in section §5.6.

The four fiducial bias parameters, b_i^B , for the B sample follow:

$$b_i^B = 2 + 2(z_i - 0.5)$$

Note that the bias at $z = 0$ is $b = 1$ in both F and B samples. This is reasonable as bias only deviates significantly from unity when the tracer is dominated by large masses or large luminosities, and this only occurs at high redshifts.

For the bright sample we focus on RSD, which corresponds to the more traditional use of a spectroscopic sample. BAO will also be considered in §6. Using a good parent photometric catalog it would in principle be possible to do WL using shear or magnitudes over the same spectroscopic objects. The gain in such case comes from the combination of galaxy positions (with good radial information) and the weak lensing information in the parent sample. This to belong to the combination FxB below and is not considered as part of the features of B sample alone. The separation will allow for a more clear understanding of what we gain with the different combinations.

4.3 Independent Samples (F+B)

Faint plus Bright: a direct combination (i.e. addition of Fisher Matrix) of the two cases above, assuming that both samples are independent and sample different parts of the sky. For a given area, the number of independent modes (or total information) available in this case is twice the number of modes for the individual samples. In this respect one should consider that F+B has twice the area or cost as F or B. But given that we will be using different probes in F and B we do not quite have twice the information.

4.4 Cross-correlation (FxB)

Faint cross Bright: samples are combined over the same area. In this case the Bright sample is a subset of the original Faint sample, but here we consider disjoint magnitude bins to have independent sets of galaxies. This will avoid mixing of systematic effects, such as photo-z transitions. The total area sampled is somehow 1/2 of the case F+B above, but we include the cross-correlations of the 2 samples for MAG (or WL) case. Here we use the MAG or WL and RSD probes in both the F and B samples as we have both adequate redshift and photometric data. Traditionally one thinks of WL probes to be applied to deep photometric samples, such as sample F. As we will show below the combination of accurate redshifts and WL information in the B sample alone produces figures of merit that can be comparable to the ones in the F sample. This information is only included in the FxB case as this involves combining the redshifts information in the B sample with the WL information in the F sample over the same objects. This only happens when we combine both samples and the B sample is a subset of the F sample over

the same area. This, together with the cross-correlation, are key and unique features of this combination.

4.5 Redshift bins

As discussed in §3.10, the redshift bin widths have little impact in the RSD analysis or shear analysis, but they are important for the galaxy-galaxy auto correlations, i.e. $C_{g_i g_i}$. We use non-overlapping top-hats with a width 4 times larger than the photo-z error in the Bright sample, i.e. $\Delta = 0.014(1+z)$. This corresponds to about 60 Mpc/h at $z = 0.6$ and is close to the smallest width where we can still neglect the intrinsic correlation between adjacent bins. For the Bright sample we will show that this width is large enough (as compared to photo-z error) so that we can almost neglect photo-z errors. For the Faint sample, which has $\sigma_z = 0.05(1+z)$, adjacent bins are strongly correlated because of photo-z errors. These correlations are taken into account in our analysis using photo-z error transitions (see §3.11), so that our results are very similar to those obtained for larger bins, as expected. Thus the equivalent effective width is much larger for the F sample than for the B sample, and is comparable to the photo-z error in the F sample. We will show in §5.7 how our conclusions depend on the redshift bin width.

5 RESULTS

In this section we will show the forecast on FoM produced by different probes on a particular choice of surveys. We will also explore how this forecast is affected by applying different assumptions on bias evolution models, photo-z errors, galaxy densities, survey areas and redshift bin-width. The goal is to understand the impact of each of the assumptions and to show how they affect the main results in this paper. We focus in MAG and RSD for most of this, but very similar results are found using other WL probes, as will also be shown. In §6 we explore different surveys, including other WL probes (Shear-Shear, Galaxy-Shear) as well as BAO in addition to MAG and RSD, and compare expected constraints for different surveys.

5.1 Bias and WL

First we explore the relation between galaxy bias, the clustering from the galaxy-galaxy autocorrelation and the clustering from the different WL probes (i.e. shear and magnification). In §5.2 RSD is added to this picture.

5.1.1 Bias fixed

Fixing the galaxy bias is the same as assuming perfect knowledge of the bias. It represents the ideal case for recovery of cosmological parameters given the galaxy samples. This case is not totally uninteresting as there are separate ways to constrain bias (i.e. from map reconstruction, halo modeling or other probes). It might also be possible to do direct lensing calibration of biasing (Bernstein & Cai 2011).

Probe/Sample	bias: free-fixed		
	FoM _w	FoM _γ	FoM _{wγ}
G-G Faint (F)	22-43	3-15	73-625
G-G Bright (B)	25-73	2-22	55-1587
G-S (B)	15-16	0.1-6	1-96
G-S+G-G (B)	26-78	4-22	108-1688
WL-all (B)	28-88	6-22	171-1940

Table 2. Figures of Merit for DE equation of state $w_0 - w_a$ (FoM_w), growth γ (FoM_γ) and joint (i.e. FoM_{wγ}). Each line shows different combinations of samples and probes: galaxy-galaxy auto-correlation (G-G), galaxy-shear alone (G-S) and their combination (excluding or including galaxy-galaxy cross-correlations). The first two entries correspond to G-G over the Faint (F) and the Bright (B) samples. In each column we show two values separated by a dash “-”. The first value (bias free) uses a fit for $b(z)$ using 4 free biasing parameters. The second assumes that bias is known (fixed bias). For 200 deg² with Planck+ SN-II priors.

Results for 200 deg² with Planck and SN-II priors are shown as the right value in the pair of numbers separated by a dash (–) in Table 2. The first two rows compare galaxy-galaxy autocorrelations (G-G) for the Faint (F) and Bright (B) samples. The Bright sample gives about a factor of 2 larger combined FoM than the Faint sample, despite having 2.5 less volume and fewer galaxies. This is because of the higher radial resolution and illustrates a key point in our approach: better radial accuracy of the foreground galaxies improve both growth and cosmic history reconstruction. Below we show (§5.7) how this changes with the number of bins (or the bin width).

The third entry is the results for galaxy-shear (G-S) in the Bright sample. Here the combined FoM_{wγ} is a factor of 15 lower than using the galaxy-galaxy autocorrelation over the same (B) sample. This illustrates the problem with weak-lensing: that has a broad kernel and is intrinsically 2D. Having good radial resolution in the foreground galaxies of the galaxy-shear cross-correlations does not help as much as in the galaxy-galaxy case (e.g. see §3.10).

The next entry shows the combination of galaxy-shear with galaxy-galaxy autocorrelation, which is still dominated by the galaxy-galaxy results, but note how there is an increase in the FoM_w due to the geometric ratios p_{ij} which are only measured in galaxy-shear. The last entry include all weak lensing and galaxy cross-correlations, including magnification (we will call this WL-all). Again here we find a significant improvement, but results seem dominated by the galaxy-galaxy auto-correlation. Note how there is very little improvement in the FoM_γ in the last two entries with respect to the galaxy-galaxy auto-correlation. When bias is known, weak lensing does not bring anything new about the growth to what we can measure with galaxy clustering alone.

5.1.2 Bias free

This picture changes dramatically when we allow bias to vary. The bold value on the left (in the pair separated by a dash) in Table 2 shows how the above results change when we measure the bias evolution $b(z)$ without priors. As justified in §2.4 we use 4 free bias parameters for each population

Probe/Sample	bias: free-fixed		
	FoM _w	FoM _γ	FoM _{wγ}
MAG (F)	23-54	5-17	113-932
RSD (B)	5-29	6-16	30-463
MAG+RSD F+B	26-137	8-25	211-3469
MAG+RSD FxB	104-199	19-31	1987-6105

Table 3. Same as Table 2 for magnification (MAG) and Redshift Space Distortions (RSD). The first two entries correspond to MAG over the Faint (F) and RSD over the Bright (B) samples. In the third row (F+B) the MAG and RSD probes over the F and B samples are combined assuming to be uncorrelated and to come from different regions of the sky. In the last line (FxB) the two samples are combined as being over the same area of the sky, including its cross-correlation and covariance.

(F or B) spaced by $\Delta a \simeq 0.1$ (i.e. $\Delta t \simeq 1Gyr$) and interpolate linearly in redshift between these 4 points.

In general, there is significant reduction in all FoMs. Notice how FoM_γ is more affected than FoM_w because bias is degenerate with growth in the power spectrum amplitude. In the case of Galaxy-Shear the FoM_w is hardly affected by the bias. Recall from Eq.58 that in this case the angular power spectrum between galaxies at redshift bin i and shear at $j > i$ is $C_{g_i\kappa_j} = b_i p_{ij} \mathcal{P}_i$. The information about $w(z)$ is encoded in p_{ij} but is also degenerate with the growth information which depends on $w(z)$ through $\Omega(z)$. This produces a degeneracy in $w(z)$ for G-S that is not broken by knowing the bias. These effects are less severe for G-G because of the better radial resolution which helps breaking this degeneracy even when bias is free. Note how in this case FoM_{wγ} is now better for the Faint sample than for the Bright sample in contrast to the situation when bias is known.

Note here how the WL-all combination (last entry) provides a significant improvement (over a factor of 3 or 1.5) in FoM_γ with respect to the G-G (B) or G-S+G-G cases. In contrast, when bias is known, where there is no improvement. This improvement comes from bias, which can be measured with the combination of galaxy-shear and galaxy-galaxy statistics, eg $b_i \propto C_{g_i g_i} / C_{g_i \kappa_j}$. This is a key point to notice. So far these results do not include the cross-correlations between the Faint and Bright samples which better exploit the complementarity of deep weak lensing measurements with good radial resolution in the foreground lenses. They also do not include RSD which provides another way to measure bias. We will explore this in the following section about magnification (MAG) and RSD and also later on (§6) when we combine all the different probes.

5.2 Combining RSD and MAG

Table 3 shows a comparison of the different FoM for MAG and RSD probes. As above, we will focus first on the results for a fixed bias.

5.2.1 Bias fixed

As shown in Table 3, RSD and MAG produce similar results for FoM_γ, while MAG is better for FoM_w. The combined

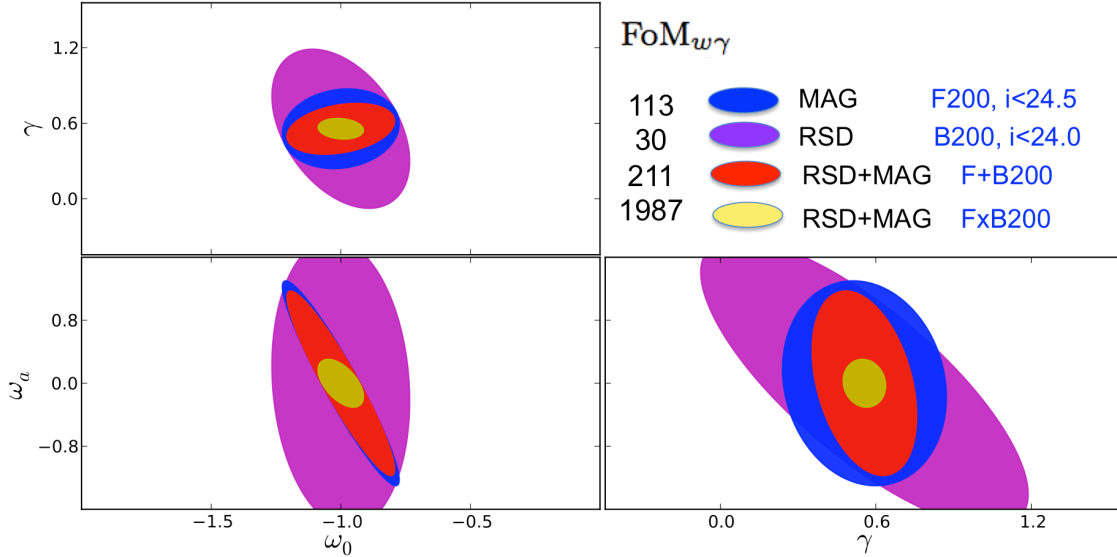


Figure 5. Contours ($\Delta\chi^2 = 2.3$) of $w_0 - w_a - \gamma$ in magnification (MAG) over a Faint sample with $22.5 < i_{AB} < 24$ (labeled F200, blue) as compared with redshift space distortions (RSD) over a bright subset (labeled B200, purple) with $i_{AB} < 22.5$ with very good photo-z resolution: $\sigma_z = 0.0035(1+z)$. Bias evolution $b(z)$ and other 6 cosmological parameters are marginalized over. The red contours correspond to the combination of both probes over different sky areas (F+B), while the yellow contours show the combination over the same area (FxB), including also all cross-correlations between galaxies in both samples.

$\text{FoM}_{w\gamma}$ is a factor of 2 better for the Faint sample using MAG.

The fact that RSD appears to be as good as MAG at measuring γ is because of the large photo-z error in the Faint sample. When we increase the photo-z accuracy MAG does much better.

One of the main points we want to stress in this paper is shown when we combine MAG+RSD. We can see a large improvement both for the separate samples (F+B) and for the cross-correlation analysis (FxB). This is highlighted by a box in Table 3. Note how the improvement is important for all FoMs.

The F+B combination improves the $\text{FoM}_{w\gamma}$ and FoM_w by factors of 3-8 and 3-4, while the gain in FoM_γ is more modest. These results will change dramatically when we allow the bias to be free.

For the F+B combination with fixed bias, having two separate samples, over different regions of the sky is worse than doing the analysis over the same region, even when we are effectively doubling the area in the first case. The difference between F+B and FxB is almost a factor of 2 for fixed bias. This is because FxB includes more observables than F+B. As explained in Section 4.4, in the FxB case we use the MAG and RSD probes in both the F and B samples and we also include the cross-correlation of the F and B samples. For F+B we only consider RSD in B, MAG on F and no cross-correlations.

5.2.2 Bias free

The above picture changes when we allow the bias to be free. In all cases the FoM degrades significantly. The degradation

depends on the sample, probe and FoM considered, as illustrated by bold numbers in Table 3. In MAG the FoM_γ degrades more than FoM_w , while the opposite happens in RSD. Note how fixing bias improves FoM_w for RSD (B). This is because of the improvement in $D(z)$ which allows $w(z)$ to be measure because it depends on $\Omega(z)$. This is in contrast with G-S in Table 2 which shows little improvement of FoM_w when bias is fixed because of further degeneracies with the lensing geometrical parameters in p_{ij} . The combination of MAG and RSD can break these additional degeneracies.

When we correlate samples over the same region of the sky (FxB) we find much better results than when the samples are independent (F+B). The improvement is about a factor of 4, 2 and 9 for FoM_w , FoM_γ and $\text{FoM}_{w\gamma}$. Bias is better constrained when both samples are over the same region as we can include the cross-correlations between them and use both MAG and RSD probes in both samples. So even when there is less information in terms of number of independent modes or total area in FxB than in F+B, there is more constraining power in the FoM of cosmological parameters. This is illustrated in Fig. 5, which shows the 3 projections (w_0, w_a, γ) in the $\text{FoM}_{w\gamma}$ ellipsoid.

For the F+B comparison there is also a significant improvement with respect to the separate F and B cases. In this case the relative improvement is smaller when bias is free (as compared to the case of known bias). It comes from having different biases for the F and B samples, but no cross measurement to relate them, as in the FxB case where we use MAG cross-correlation to relate the bias in F and B.

Allowing the bias to be free reduces the combined $\text{FoM}_{w\gamma}$ by factors of 8 and 15 in MAG and RSD. But this re-

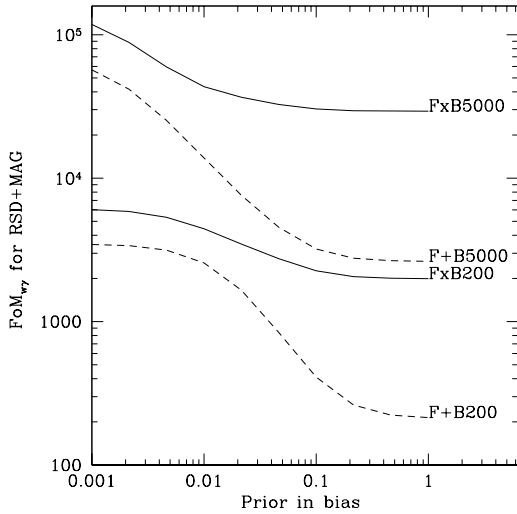


Figure 6. $FoM_{w\gamma}$ in the MAG+RSD combination as a function of priors in the bias parameters (absolute rms error). Dashed lines corresponds to the FoM when we combine samples from different regions of the sky (F+B), while continuous lines correspond to the cross-correlation of samples over the same area (FxB). Upper/lower lines corresponds to 5000/200 deg^2 surveys.

duction is only a factor of 3 for the FxB combination. These results assume no priors on bias. Next we will see how this changes when we have some priors on bias.

5.3 Priors on bias

Figure 6 shows how the $FoM_{w\gamma}$ increases as we reduce the priors in the bias parameters. These priors can come from other observations or from modeling of bias (e.g. see §2.4). The same gaussian prior is used for all the bias parameters. F+B adds MAG in the F sample with RSD in the B sample, while FxB include all combinations and cross-correlations. The figure shows that the FxB combination is less affected by priors than the other combinations and reflects the fact that bias is better measured by the FxB combination. A prior of 0.01 in bias improves the FoM of FxB and F+B by about a factor of 1.5 and 5 respectively for the 5000 deg^2 sample. With such priors, the FxB combination still has a $FoM_{w\gamma}$ that is 4 times larger than F+B. This is because in for the FxB combination we use both RSD and WL over the bright and faint sample, while in F+B we only use RSD over B and WL over F.

Also note how for no priors the FoM in the small sample combination FxB200 is almost as good as the F+B5000 combination which has 25 times larger area.

If we use 2 biasing parameters per population instead of 4 to describe $b(z)$ (i.e. see §2.4) we find an increase of about 40% in the FxB combined $FoM_{w\gamma}$ for both 200 or 5000 deg^2 samples.

We conclude that the impact of bias evolution is well understood and our results are quite robust with respect bias modeling.

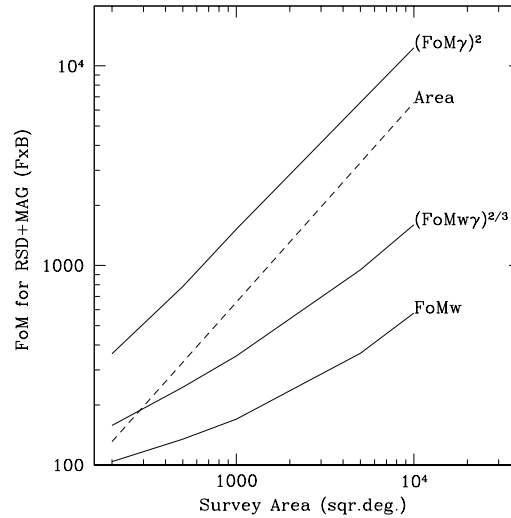


Figure 7. Variation of the different FoM: FoM_γ^2 (top line), $FoM_{w\gamma}^{2/3}$ and FoM_w (bottom line) as a function of the Survey Area. This is RSD+MAG combined over the same area (FxB). The dashed line shows the scaling with area for reference.

5.4 Survey Area

Figure 7 shows how the MAG+RSD combination over the same area (FxB) changes as a function of the survey area. For the Fisher Matrix without priors we expect the following scaling: $FoM_w \propto A$, $FoM_\gamma \propto A^{1/2}$ and $FoM_{w\gamma} \propto A^{3/2}$, according to Eq.14, as it depends on the number of parameters in each FoM definition. The values shown in Fig.7 are rescaled accordingly and show the FoM corresponding to the geometrical mean of the parameters involved. After this rescaling, they should all scale linearly with the area. But we are using Planck and SN-II priors which tend to dominate the results for smaller area, resulting in a weaker dependence in A . A fit to Fig.7 yields:

$$FoM_w \propto A^{0.44} \quad (83)$$

$$FoM_\gamma \propto A^{0.45} \quad (84)$$

$$FoM_{w\gamma} \propto A^{0.89} \quad (85)$$

Note that FoM_γ^2 is larger than FoM_w , which indicates that γ is better determined than the geometrical mean of w_0 and w_a . This is despite the fact that we include Planck and SN-II priors, which include priors in w_0 and w_a , but no priors in γ .

5.5 Bright Magnitude limit

Figure 8 shows how the FoM changes as we change the magnitude limit (m_l) of the bright sample. For $N(z)$ we use the distributions shown in Fig.4. The combined $FoM_{w\gamma}$ for MAG in the Bright sample depends strongly on m_l , as shown by the bottom lines in the figure, for both 200 and 5000 deg^2 . When combined with the Faint sample and RSD, the dependence is weaker. For the later case we find:

$$FoM_{w\gamma} \propto 1.4^{m_l} \quad (86)$$

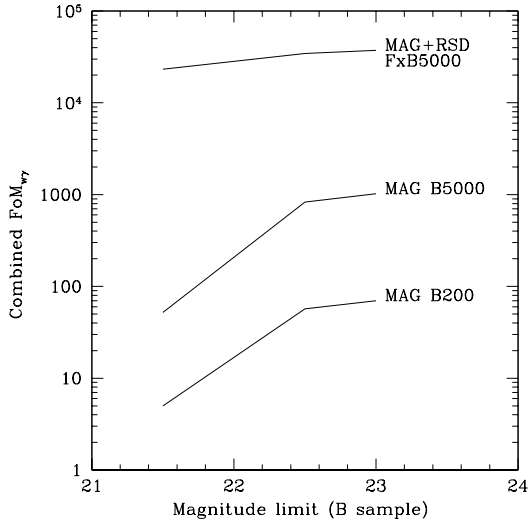


Figure 8. Lines show the combined $\text{FoM}_{w\gamma}$ as a function of the magnitude limit of the bright sample for different samples and probes, as labeled. The top line corresponds to the FxB cross-correlation using both MAG and RSD. The lower lines correspond to MAG alone over the Bright sample with 5000 deg^2 or 200 deg^2 .

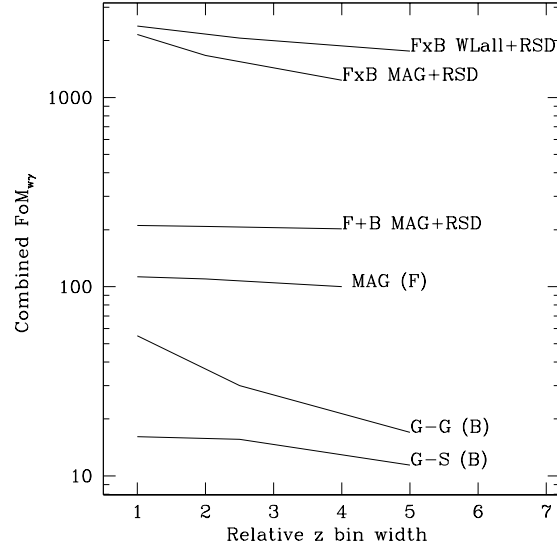


Figure 10. Combined $\text{FoM}_{w\gamma}$ as a function of the relative redshift bin width (with respect to the fiducial value of $0.014(1+z)$) for the different samples and probes. As usual, F+B adds MAG in the F sample with RSD in the B sample, while FxB include all combinations and cross-correlations.

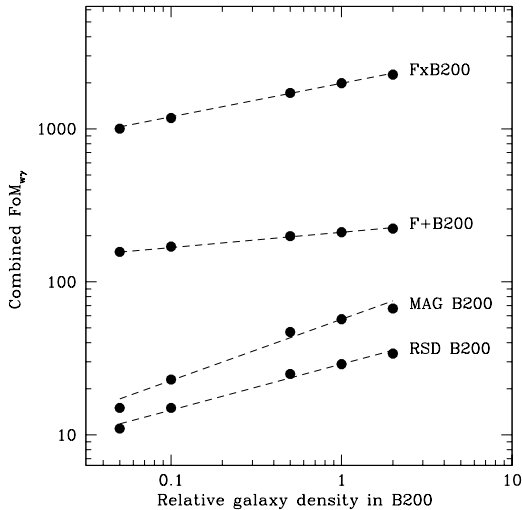


Figure 9. $\text{FoM}_{w\gamma}$ as a function of the relative galaxy density \bar{n} in B200 with respect to the fiducial values (in §4) for different probes, as labeled. As usual, F+B adds MAG in the F200 sample with RSD in the B200 sample, while FxB include all combinations and cross-correlations. The dashed lines show a fit to \bar{n}^β .

5.6 Shot-Noise

What happens if we reduce or increase the galaxy density? The bright sample ($m_l < 22.5$), for which we so far have assumed a PAU-like survey measuring low resolution spectra for most of the galaxies, likely has a lower density for a truly spectroscopic survey. A different density can also come from only considering a subset of the data or dividing the galaxies in types.

Figure 9 shows how the FoM from the different probes changes as we reduce (or increase) the density in the bright sample with 200 deg^2 (B200). The dilution is given in terms of the default density in §4, which already corresponded to a 50% completeness. Both RSD and MAG are quite affected by sample dilution, especially when we approach values lower than 10% completeness. The data can be fitted with a power-law in the relative density \bar{n}^β , with $\beta \simeq 0.3$ for MAG and $\beta \simeq 0.4$ for RSD (dashed lines in the figure). It is therefore important to keep a high density if we want a high FoM.

The effect is less severe in the F+B200 combination ($\beta \simeq 0.1$) because the density of the faint sample (F200) is kept constant. For the FxB200 combination the effect is in between the one for B200 and the one for F+B200. The effect of dilution in the FxB200 case can be well described as:

$$\text{FoM}_{w\gamma}^{\text{FxB}} \propto \bar{n}^{0.22} \quad (87)$$

5.7 Redshift bin width

Figure 10 shows how the $\text{FoM}_{w\gamma}$ changes when we change the redshift bin width from 4 to 20 times the photo- z error in the Bright sample, i.e. 1 to 5 times the fiducial values.

Changing the bin width has little effect on the Faint sample for MAG. The fiducial z -bin, $0.014(1+z)$, is already smaller than the photo- z error in the Faint sample, $0.05(1+z)$, so that nearby bins are strongly correlated. Increasing the bin width by a factor of 4 only changes $\text{FoM}_{w\gamma}$ by 12%. This illustrates that the method to account for transition probabilities in §3.11 and their covariance in §3.9, properly take into account the impact of photo- z errors in

the MAG forecast. We do expect some small degradation as we increase the redshift bin width because of the lost of radial information. This degradation is more significant for a bin width which is larger than the photo-z error.

For the Bright sample different redshift bins are independent as they are at least 4 times larger than photo-z error. The impact of changing the bin widths is quite different for RSD and MAG. For RSD the results are independent of the bin size, once there are enough bins. This is because we are using 3D information within each bin to measure the distortions: this is possible because we are in the linear regime and we assume photo-z accuracy that is good enough for this task, see §2.5. The redshift bin slicing only affects the radial resolution in the parameter estimation, but it does not add new modes as happens when we do 2D clustering. So as long as there are enough bins to capture the slow cosmic evolution the results are unchanged in 3D. The F+B case suffers little degradation because it is just the sum of F with MAG and B with RSD, neither of which changes with number of bins.

For MAG in the Bright sample the effect is more important because the result is dominated by the 2D galaxy-galaxy (G-G) correlations (see Table 2), whose signal-to-noise depends linearly in the number of redshift bins (see §3.10). If we reduce the number of independent bins, we directly reduce the FoM. In the case of MAG for the Bright sample a bin width that is twice as large reduces the $FoM_{w\gamma}$ by a factor of two. This agrees with the reduction of the 2D G-G FoM for the B sample shown in Fig. 10. Note how the degradation is much smaller in the G-S because its signal-to-noise is independent of the number of bins (see §3.10).

The influence of the 2D galaxy-galaxy contribution is also apparent in the top lines of Fig. 10, which shows that the FxB combination for MAG or for WL-all (which includes all galaxy and Shear correlations) As we decrease the redshift bin width by a factor of 5, the combine FoM of FxB in MAG+RSD increases by 75%.

Overall, this illustrates well one of the main points we want to stress in this paper: that the benefit of the FxB combination comes from the combination of many independent redshift bins.

5.8 Photo-z errors

Figure 11 shows how the combined $FoM_{w\gamma}$ changes as we change the relative photo-z errors, σ_z , in the bright sample. Here the photo-z error distribution is Gaussian.

The variation on $FoM_{w\gamma}$ is smaller for MAG than for RSD. This makes sense as the bright MAG analysis uses relatively broad redshift bins: $\Delta_z = 0.014(1+z)$, i.e. 4 times the nominal photo-z error of $\sigma_z = 0.0035(1+z)$. This makes our result conservative but quite insensitive to photo-z errors. In the case of RSD the degradation comes from the S/N reduction on modes affected by the photo-z error.

For the FxB results the effect is less severe as here we also include results for the faint sample for which the photo-z error is fixed. These tendencies can be fitted to an exponential decrease: $e^{-A\sigma_z^2}$. For both the 200 and 5000 deg² we find that to a good approximation:

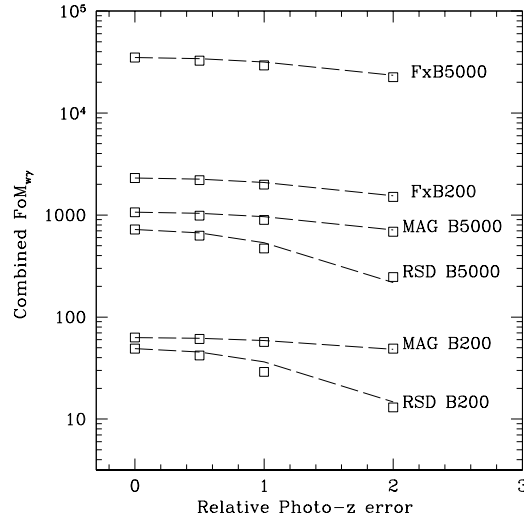


Figure 11. Symbols show the combined $FoM_{w\gamma}$ as a function of the relative photo-z of the bright sample (with respect to the fiducial values in $\sigma_z = 0.0035(1+z)$) for the different samples and probes, as labeled. Dashed lines show the best fit to $e^{-A\sigma_z^2}$.

$$FoM_{w\gamma}^{FxB} \propto e^{-0.1[\sigma_z/0.0035(1+z)]^2} \quad (88)$$

$$FoM_{w\gamma}^{RSD} \propto e^{-0.3[\sigma_z/0.0035(1+z)]^2} \quad (89)$$

These fits are shown as dashed lines in the figure. MAG in the B200 sample falls a bit less steeply ($A \simeq 0.07$) than MAG in the B5000 ($A \simeq 0.1$).

Note in Figure 11 how, despite having 25 less area, the combined FxB200 result is better than the separate MAG or RSD results over B5000. This is also true for results over the F5000 sample.

5.8.1 Uncertainties in photo-z transitions

So far we have considered the case where we know perfectly well how photo-z uncertainties change the observables. This corresponds to the case $\Delta_r = 0$, where Δ_r is our uncertainty in the fraction of galaxies r_{ij} that are wrongly allocated to a given redshift bin, as defined by Eq.78. The left panel in Fig.12 shows how the FoM for Magnification (MAG) and Shear-Shear cross-correlations (Shear) degrades as we increase the absolute error Δ_r . In the left panel we only include WL probes and no RSD.

For MAG, the degradation in the FoM is similar for the Bright and Faint samples. In the limit of small errors in r_{ij} the FoM of MAG is not so different for the Faint and the Bright sample, despite the fact that the former is much deeper, has more redshift range, volume and galaxies. This is because of the better radial resolution in the Bright sample that almost compensates for its smaller volume. As we increase the uncertainties in the photo-z transitions the FoM degrades quickly, as we lose the capacity to locate radial bins.

Recall that the Faint sample has a much larger photo-z

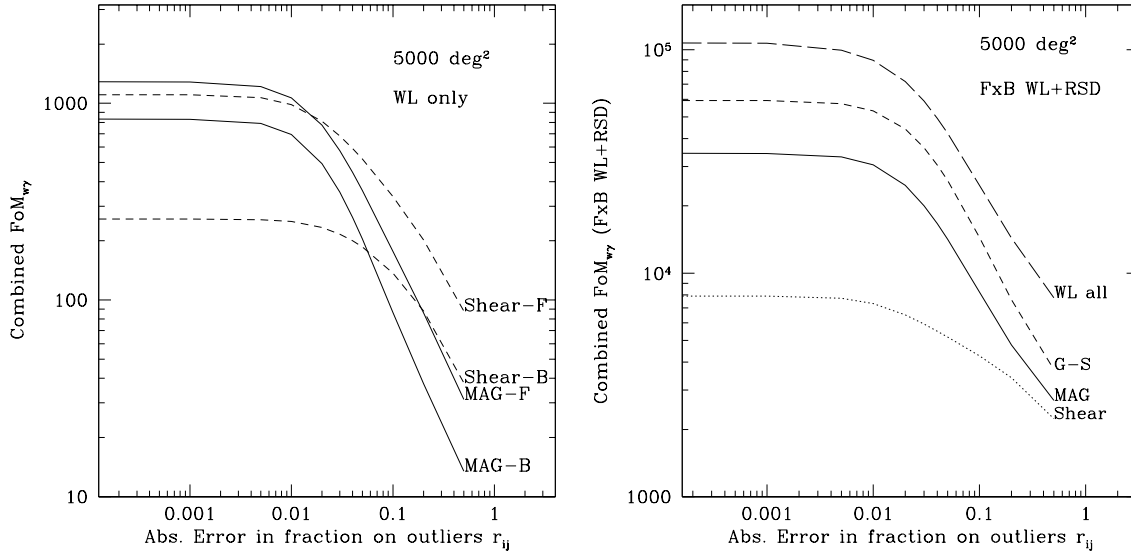


Figure 12. Combined $\text{FoM}_{w\gamma}$ as a function of the absolute error in our knowledge of the photo- z transitions for 5000 deg^2 survey. LEFT: Results correspond to cosmic magnification (MAG, continuous lines) or Shear-Shear cross-correlation (Shear, dashed lines) alone, i.e. without RSD, for both the Faint (F) and Bright (B) samples. RIGHT: Results correspond to the FxB cross-correlation of the F and B sample, including RSD with different WL probes: magnification (MAG, continuous lines), Galaxy-Shear cross-correlations (G-S, short-dashed), Shear-Shear cross-correlation (Shear, dotted line) and all WL combined (long dashed lines). When photo- z transitions are known to better than about 1% there is no significant degradation in the FoM.

error than the Bright sample and therefore the fraction of galaxies r_{ij} will also be much larger. This means that for a fix absolute error in r_{ij} the relative error will be much smaller for the Faint sample. Does it make sense then that the FoM is degraded equally for the Faint and Bright sample, as shown in Fig.12?

As discuss in §5.7 results for MAG in the Faint sample depends very weakly on the redshift bin width as long as it is not much larger than the photo- z error. To understand our new results we can increase the bin width in the Faint sample to make it similar or slightly larger than its photo- z error. We then have that for both the Faint and Bright sample $r_{ii} \simeq 1$ and $r_{ij} < 1$ for $i \neq j$. In this case, the variance in C_{ij} caused by an absolute error Δ_r in r_{ij} is:

$$(\Delta C_{ij})^2 \simeq \Delta_r^2 (C_{ii}^2 + C_{jj}^2) \quad (90)$$

This should be compared to the variance in C_{ij} in Eq.59. In the limit $C_{ii} \simeq C_{jj} > C_{ij}$ we have:

$$\frac{(\Delta C_{ij})^2}{\text{Cov}[C_{ij}; C_{ij}]} \simeq 2\Delta_r^2 N(\ell) \quad (91)$$

which is independent of C_{ij} and therefore of σ_z .⁷ If we want this ratio to be smaller than 1/4, so that the error in C_{ij} is not dominated by Δ_r , we find that we need $\Delta_r < 10^{-2}$ for $\ell \simeq 300$, which is in good agreement with Fig.12 and illustrates why this result is the same for the F and B sample, and why its shape is also independent of the redshift

⁷ If we include shot-noise we have to divide this by a factor $[1 + 1/(\bar{n}C_{ii})]^2$ which is typically of order unity, but depends weakly on the sample and redshift bin width.

bin width. We have checked this prediction by redoing the results on the left panel of Fig.12 for twice the bin width. For the Faint sample we find a very similar result with a $\text{FoM}_{w\gamma}$ that is only 5% lower for the larger bin width for all values of Δ_r . For the Bright sample the results are a factor of 2 lower, as expected from §5.7, with a similar shape as function of Δ_r .

For absolute errors larger than about 1%, the degradation for the shear-shear cross-correlation (dashed line labeled Shear in left panel of Fig.12) is smaller than for MAG. This is because MAG provides better constraint than Shear alone. Despite the additional parameters from biasing, MAG always has a larger FoM than Shear for $\Delta_r < 1\%$ because of its better radial resolution. This is specially true for the Bright sample, which also has too small a volume to take advantage of shear. But because of the broad radial resolution, the FoM from Shear is less sensitive to the uncertainties in the photo- z transitions. Note that this formalism for degradation is more general (for narrow bins) than the one based on the uncertainties in the centroid position of the photo- z source distribution (eg Huterer et al 2006).

The FoM for MAG using a bright (B) sample with spectroscopic or good (better than 1%) error in r_{ij} is a few times larger than for MAG or Shear-Shear over a deeper (F) sample with low photo- z accuracy (i.e. $\simeq 10\%$ error in r_{ij}). When the accuracies are similar for both samples the situation reverses. With 200 deg^2 survey the results follow the same trend.

For the MAG probe, we need to know the transitions to better than 4% (1%) if we want the FoM to degrade less than 50% (11%). This is the case for both the Faint and Bright

200 deg² samples. For the 5000 deg² samples we need to know the transitions to better than about 2.5% (1%) if we want the FoM to degrade less than 50% (17%). A bright sample with 5000deg² where we only know transitions to 20% gives similar FoM as a sample with only 200deg² where transitions are known better than 2%.

The relative impact in the FoM is similar if we consider combined probes with RSD, which we have assumed is not affected by uncertainties in the photo-z transitions. This is illustrated in the right panel of Fig.12, which shows the corresponding results for the FxB combination of RSD with different WL probes. Here we take Δ_r to be same for the F and B sample, which is probably pessimistic for bright spectroscopic samples (but not for PAU-like surveys). The short-dashed line corresponds to the Galaxy-Shear (G-S+G-G) cross-correlation (which also includes the galaxy-galaxy autocorrelation $C_{g_i g_i}$) while the continuous lines correspond to MAG (i.e. $C_{g_i g_j}$). The dotted line shows the shear-shear results. The long dashed line combines (with appropriate covariance) all WL lensing probes (ie MAG, G-S, G-G and S-S). As can be seen in the figure, both MAG, G-S+G-G and combined probes are affected in a very similar way by the uncertainty in the photo-z transitions. As before, shear-shear is less affected by this uncertainty, but gives a much lower FoM. The degradation here is only slightly lower than in the previous case, where we did not include RSD. When the uncertainty in the bin transition Δ_r are less than 0.1 we find:

$$FoM_{w\gamma}^{FxB} \propto e^{-(\Delta_r/0.18)(A/200)^{0.05}} \quad (92)$$

where A is the survey area in deg². The A dependence reflects the fact that to achieve a given FoM degradation we need to know the transitions around 15% better (i.e. Δ_r should be 15% lower) for $A=5000$ deg² than for $A=200$ deg². This makes sense, as the errors are lower for $A=5000$ deg², so the requirements should be higher. Accuracies of few percent in r_{ij} seem within reach with current or near future photo-z codes with appropriate calibration, so this is not a critical limitation to measure magnification.

Note how the FoM can increase by over a factor of 100 when we cross-correlate the samples and include RSD, i.e. compare the values of the FoM of FxB in the right panel with the FoM of F or B separately in the left panel.

5.8.2 Non-Gaussian transitions

We have also explored the case of non-Gaussian transitions by running a photo-z code over galaxy simulations and exploring how this change the results with respect to the Gaussian case. We have estimated the photo-z transitions r_{ij} using the photo-z code over mock galaxy simulations. Details of this study will be presented elsewhere. Here we just want to point out that in many cases we find that surprisingly the FoM increases for the Non-Gaussian transitions compared to the Gaussian case. The reason for this is that for the Gaussian comparison we use a gaussian rms σ_z corresponding to the the 68% CL of the photo-z distribution in simulations. The actual (non-Gaussian) photo-z distribution

Probe/Sample	FoM _w	FoM _γ	FoM _{wγ}
FxB no wiggles	90 (1.42)	18.7	1692 (20.1)
FxB wiggles	104 (2.89)	19.1	1988 (37.1)
F+B no wiggles	26.1 (0.25)	8.1	211 (1.98)
F+B wiggles	25.6 (0.39)	8.1	208 (2.36)

Table 4. Impact of having BAO wiggles in the MAG+RSD combination for 200deg² survey with Planck and SN-II priors. Results without priors are in parentheses.

is often much sharper in the center and has longer tails than a Gaussian. If the distribution is known, this results in a better radial resolution and therefore better FoM. In reality this improvement is limited by our uncertainties in the photo-z distribution (see §3.12 and below).

5.9 Impact of BAO wiggles

The BAO wiggles in $P(k)$ can be measured in the angular galaxy-galaxy correlations when we use narrow redshift bins. We test this by comparing results using the standard Eisenstein & Hu (1998) $P(k)$ with and without the BAO feature for the same cosmology.

Results for MAG+RSD are shown in Table 4. There is no impact on RSD as the shape is fixed in this case. The combined FoM in MAG+RSD (FxB) increases by about 18% due to this effect. Of course this change mostly affects $w(z)$ FoM as γ is measured by the amplitude and not the shape of $P(k)$. Note how the F+B combination increases by less than 2% compared to 18% in FxB. This reflects the fact that the F+B combination does not measure the shape as well as the FxB combination. Recall that in F+B we use MAG for the faint sample alone, which has low radial resolution, which translates into a lower resolution in k for the shape measurement.

The effect in FoM_w with priors is 15% for FxB and 2% for F+B. In parentheses we also show the results without priors. In this case the FxB combination increases by a factor of 2 in FoM_w when wiggles are included. For F+B the gain is almost 60%. We find very similar relative improvement for 5000deg²: without priors FoM_w in FxB5000 goes from 185 to 361 when including the wiggles. These are quite substantial gains and illustrate that the BAO wiggles are indeed measured with these probes.

5.10 Degeneracies

We investigate here the gain in the MAG+RSD (FxB) combination for different parameters. Table 5 shows how the FoM_{wγ} (with Planck and SN-II priors) degrades when we add a new parameter. We see how the bias parameters are the ones where the MAG+RSD combination degrades less than the separate RSD and MAG. So they are the ones that benefit most from the MAG+RSD combination. For example note how allowing b_1 , the bias at the lower redshift of $z_i = 0.25$, to vary causes the FoM to degrade by 30-50% for RSD or MAG separately but only by 4-6% for the FxB combination.

In some cases, like n_s , the degradation increases when

Parameter	MAG	RSD	MAG+RSD
Ω_m	32.5	76.2	32.5
Ω_{DE}	62.9	69.2	58.1
Ω_b	27.7	75.8	43.5
h	35.2	76.0	39.2
n_s	0.3	0.0	32.4
σ_8	0.0	0.9	0.6
b_1^F	43.6	28.4	4.8
b_1^B	47.3	31.9	5.8
b_2^F	53.3	40.5	10.3
b_2^B	57.7	46.0	12.5
b_3^F	71.8	66.7	32.2
b_3^B	71.6	67.7	31.9
b_4^F	72.1	79.7	44.3
b_4^B	68.9	78.3	40.6

Table 5. Degradation (per cent reduction) of the FoM $_{w\gamma}$ when we add a new parameter to the FxB200 cross-correlation forecast. The change is relative to the case where we have all parameters varying except for the one quoted (without priors). The 4 bias parameters for the Faint and Bright populations b_F and b_B are the parameters that gain most in the MAG+RSD combination.

we consider the combined RSD+MAG probes. This is because the result for separate probes is dominated by the priors. In this case adding a new parameter does not degrade the FoM. The combination of probes provide better constraints which are no longer dominated by priors. This results in an increase in degradation. In the case of σ_8 , the degradation is always low as its value is dominated by priors and does not affect much our FoM.

5.11 Marginalized errors

Table 6 shows the marginalized 1-sigma error-bars of different parameters for each probe. This corresponds to 200 deg² with Planck and SN-II priors. The table reflects in other parameters what we have already found for the different FoMs: that the FxB probe provides improvements in errors by factors of a few with respect to the errors in separate MAG or RSD probes. In particular note how the error in bias goes from $\simeq 5-8\%$ to $\simeq 1-2\%$. The error in σ_8 does not change as is dominated by priors. This is fine as our goal is to measure the growth evolution and not the overall normalization.

6 SURVEY COMPARISON

Table 7 shows a comparison of different surveys and probes. In the upper section of Table 7 we compare different WL probes for the parent F5000 photometric sample. The following entries correspond to probes for the brighter spectroscopic samples, smaller area surveys and different probes either combined over different areas or cross correlated.

6.1 Shear-Shear, Galaxy-Shear and MAG

In the first three entries in Table 7 we compare MAG with Galaxy-Shear (G-S+G-G) and Shear-Shear (S-S) using the same assumptions, fiducial model and priors for a 5000 deg² survey. Using S-S, $C_{\kappa_i \kappa_j}$, is the most conservative use of WL

Parameter	MAG	RSD	MAG+RSD	MAG+RSD
	F	B	F+B	FxB
Ω_m	2.4%	47%	2.4%	1.6%
Ω_{DE}	1.3%	9.2%	1.3%	0.9%
h	1.3%	24%	1.3%	0.8%
σ_8	0.9%	0.9%	0.9%	0.9%
n_s	0.65%	0.66%	0.65%	0.61%
Ω_b	2.7%	47%	2.7%	1.8%
w_0	15%	17.5%	14%	5.8%
w_a	0.86	1.20	0.77	0.20
γ	37%	74%	24%	9.7%
b_1^F	4.2%	-	3.7%	1.6%
b_1^B	-	5.1%	4.2%	1.5%
b_2^F	4.9%	-	4.0%	1.6%
b_2^B	-	4.6%	3.5%	1.6%
b_3^F	6.3%	-	4.2%	1.7%
b_3^B	-	5.9%	4.7%	1.6%
b_4^F	4.9%	-	3.3%	1.7%
b_4^B	-	8.7%	9.4%	1.8%

Table 6. Marginalized error-bars for each parameter and different probes. For 200 deg² with Planck and SN-II priors.

as it does not require any galaxy biasing modeling. Note that in G-S+G-G we also include the galaxy-galaxy auto-correlations, i.e. it includes both $C_{g_i k_j}$ and $C_{g_i g_i}$, but does not include S-S, $C_{\kappa_i \kappa_j}$, or galaxy cross-correlation, $C_{g_i g_j}$, for $i \neq j$. Magnification (MAG) includes both auto and cross-correlations, i.e. $C_{g_i g_j}$, for all i and j . As expected the MAG result for F5000 is in-between the S-S and the G-S+G-G. Despite the need of the biasing parameters and the relatively poor radial resolution, $\sigma_z = 0.05(1+z)$, G-S+G-G and MAG still make better use of the radial information than S-S. The galaxy-shear cross-correlation alone, i.e. C_{gk} , has lower noise than MAG, i.e. C_{gg} , as can be seen in the covariance of Eq.59:

$$Cov(C_{gg}, C_{gg}) \propto C_{gg} C_{gg} \quad (93)$$

$$Cov(C_{gk}, C_{gk}) \propto C_{gg} C_{kk} \quad (94)$$

where C_{kk} is much smaller than C_{gg} . This means that without noise G-S performs better than MAG. But systematic effects will be quite different for measuring accurate shapes versus accurate photometry. It is also likely that in practice there are higher densities of galaxies available for MAG than for Shear as we move to higher redshifts and this has not been taken into account here.

An advantage of our approach is that we can include all observables in the same FM (with appropriate covariances) to provide a joint analysis of MAG+G-S+G-G+S-S including all covariances (label WL-all in the Table). The WL-all case (entry 4 in the Table) includes all these weak lensing probes, and of course gives the best results. The improvement of WL-all over G-S+G-G is almost a factor of 3: compare entries #4 and #3. This is due to the direct measurement of the matter amplitude (ie growth) by S-S which helps breaking degeneracies with bias in G-S+G-G and MAG.

#	Probe	Sample	η Completeness	Volume Gpc ³ /h ³	$\sigma_z/(1+z)$ Photo-z error	FoM _w γ free	FoM _{γ}	FoM _{wγ} $\times 10^3$
Photometric $22.5 < i_{AB} < 24$								
1	Shear-Shear (S-S)	F5000	1/2	18	0.05	46	24	1.1
2	Magnification (MAG)	F5000	1/2	18	0.05	53	24	1.3
3	Galaxy-Shear (G-S+G-G)	F5000	1/2	18	0.05	129	27	3.5
4	All Weak Lensing (WL-all)	F5000	1/2	18	0.05	220	41	9.1
Spectroscopic $i_{AB} < 22.5$								
5	MAG	B5000	1/2	7	0.0035	79	11	0.8
6	RSD	B5000	1/2	7	0.0035	27	17	0.5
7	RSD	B5000spec	1/20	7	0	20	17	0.3
8	RSD	B5000spec21.5	1/26	3.5	0	10	16	0.2
9	BAO	B5000	1/2	7	0.0035	47	-	-
10	BAO	B5000highz	1/10	18	0	78	-	-
Small Area: 200 deg ²								
11	MAG+RSD	FxB200	1/2	0.7	0.05-0.0035	104	19	1.9
12	G-S+G-G+RSD	FxB200	1/2	0.7	0.05-0.0035	126	19	2.4
13	WL-all+RSD	FxB200	1/2	0.7	0.05-0.0035	156	22	3.5
Combined as Independent								
14	BAO+RSD	B5000highz	1/10	18	0	100	27	2.7
15	BAO+WL-all	F+B5000highz	1/2-1/10	7-18	0.05-0	285	41	12
16	BAO+RSD+WL-all	F+B5000highz	1/2-1/10	7-18	0.05-0	334	56	19
17	MAG+RSD	F+B5000	1/2	7-18	0.05-0.0035	76	37	2.9
18	WL-all+RSD	F+B5000	1/2	7-18	0.05-0.0035	270	58	16
19	WL-all+RSD	F+B5000spec	1/2-1/20	7-18	0.05-0	264	57	15
Cross-correlation								
20	MAG+RSD	FxB5000	1/2	7-18	0.05-0.0035	426	81	34
21	WL-all+RSD	FxB5000	1/2	7-18	0.05-0.0035	1120	96	107
22	WL-all+RSD	FxB5000spec	1/2-1/20	7-18	0.05-0	1036	92	95
23	WL-all+RSD	FxB5000spec21.5	1/2-1/26	3.5-18	0.05-0	610	71	43

Table 7. FoM comparison for different surveys and probes: Shear-Shear (S-S), Galaxy-Shear (G-S+G-G, which includes Galaxy-Galaxy autocorrelations), Magnification (MAG), redshift space distortions (RSD) and Baryon Acoustic Oscillations (BAO). The WL-all case includes MAG, S-S, G-G and G-S. All samples are 5000deg² except for #11-13 which are 200deg². The 5th column gives the comoving volume to the highest redshift used in each analysis. BAO alone (#9-10) does not provide FoM _{γ} or FoM_{w γ} .

6.2 Bright spectroscopic samples

As defined in §4 the B5000 sample is close to spectroscopic as it has very good photo-z, $\sigma_z = 0.0035(1+z)$, but a very high completeness (of 10000 galaxies/deg² to $i_{AB} < 22.5$). This is motivated by the PAUCam concept (see §1), but we also show results for more standard (future) spectroscopic flux limited samples. One of them is called B5000spec: it has $\sigma_z = 0$ and 1000 galaxies/deg². Otherwise B5000spec is identical to B5000. A second sample is called B5000spec21.5 is flux limited to $i_{AB} < 21.5$ (instead of $i_{AB} < 22.5$ in B5000spec or B5000) with only 500 galaxies/deg². This gives a mean redshift of 0.4 and about half the volume of $i_{AB} < 22.5$ (see also long dashed line in Fig.4). As shown in Table 7 (comparing entries 6-7), the RSD results for B5000spec are lower than for B5000, indicating that density is more important than spectroscopic accuracy as found in §5.6 and §5.8. This is a good validation of the PAUCam concept. The result for B5000spec21.5 is almost a factor of 2 lower, but still quite competitive given that it will be much faster to get spectra for galaxies which are 1 magnitude brighter.

When the B5000 sample is a subset of F5000 (i.e. in the FxB case) we can also estimate MAG for B5000 as we will have both good redshift accuracy and good photometry

to do shear or magnification. This is shown as entry #5 in Table 7. Note how MAG over B5000 provides slightly better FoM_w and only slightly lower FoM_{w γ} than MAG over F5000, despite the larger volume and depth in F5000. This of course is due to the better resolution in the radial bins.

BAO is also included in our forecasts for comparison. We follow the method of Seo & Eisenstein (2007) using the same fiducial values and parameters as for the other cases (see §2.3). We consider two different surveys for a BAO follow-up of F5000. The usual B5000, which for FxB can be considered a brighter subset of F5000 and therefore lies in its foreground, with most of the redshifts at $z < 0.5$. the other is B5000highz which corresponds to a selection (e.g. emission line galaxies) which is biased towards higher redshift targets out of F5000, with around 2000 galaxies/deg², used to maximized the BAO probe. We use a constant number of target galaxies per unit redshift in the range $0.2 < z < 1.7$ which has about 2.5 larger volume than B5000. The BAO result for B5000highz is about a factor of 2 better than for B5000, as expected. This is about the largest BAO FoM that one could get based on targets from the parent F5000 sample as we have assumed it covers the same volume as F5000 and has quite a large density. The result is almost as large as the FoM_w for MAG in B5000 (entry #5), but note

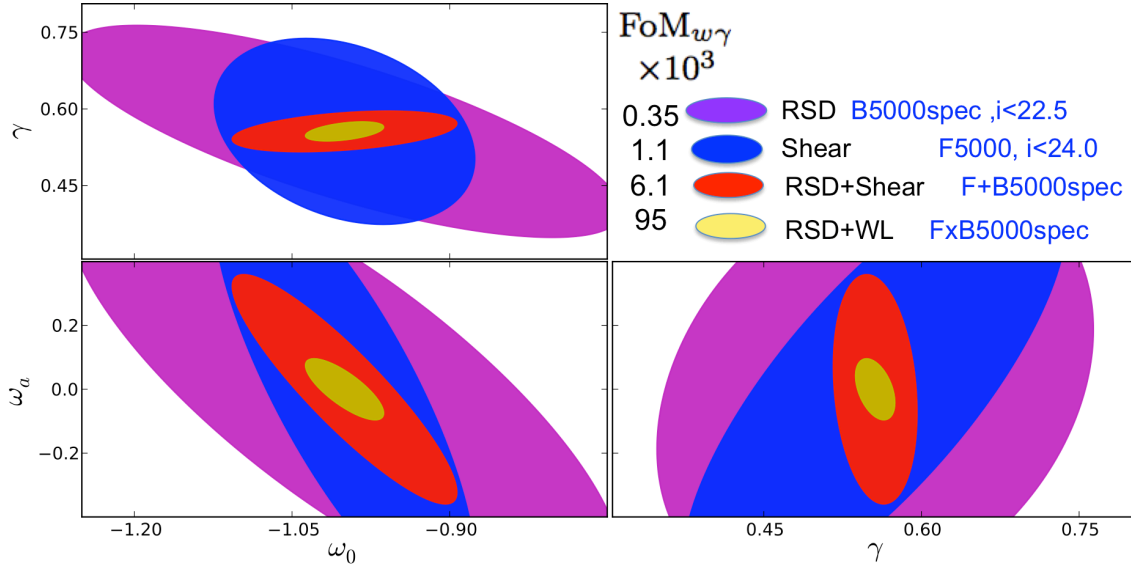


Figure 13. Contours ($\Delta\chi^2 = 2.3$) of $w_0 - w_a - \gamma$ in weak lensing (only Shear-Shear) over a Faint sample with $i_{AB} < 24$ (F5000, blue) as compared with RSD over a bright spectroscopic subset (B5000spec, purple) targeting 1000 galaxies per square degree to $i_{AB} < 22.5$. Bias evolution $b(z)$ and other cosmological parameters are marginalized over. The red contours correspond to the combination of both probes over different sky areas (F+B), while the yellow contours show the combination over the same area (FxB), including also all cross-correlations between shear and galaxies in both samples. This produces over a factor 10 larger combined FoM.

that with MAG we can also measure γ , which is not possible with BAO. As mentioned earlier, doing MAG over B5000 is in fact only a subset of what we can do when we combine the good radial resolution in B5000 with the photometrical (and WL) information in F5000, i.e. the FxB combinations which will be discussed next.

6.3 Smaller area surveys

In the 11th-13th rows of Table 7, we see how a modest survey, with only 200 deg^2 can give a better FoM based on cross-correlation (FxB200 in the table) than much larger surveys (F5000 or B5000) that consider only either MAG, S-S, G-S, RSD or BAO separately, i.e. all entries above in Table 7, except entries #3 and #4 which combine several probes. In particular, the BAO PAU Survey proposed in Benitez et al. (2009) with 5000 deg^2 yields a $\text{FoM}_w = 47$ (entry #9 in the Table) which is a factor of 2-3 times smaller than the combination of RSD with MAG (or WL probes) over 200 deg^2 (entries #11-13). This represents a factor of 50-70 improvement in the ratio of benefit over cost, if we assimilate cost with area and benefit with FoM. In addition, the RSD+WL-all cross-correlation also provides constraints on γ of about 5% accuracy, which cannot be obtained from BAO.

If we combine the Fisher matrix of MAG and RSD from two large surveys (F+B5000) we do better than FxB200, but not by far. When we include all WL and RSD in the F+B5000 combination (row #18) the improvement is more significant, overcoming the FxB200 result by a factor of 4. As the combined FoM scales roughly with the area (Eq.85), doing $\sim 800 \text{ deg}^2$ with the FxB cross-correlation will pro-

vide similar combined FoM than the combination of the two larger but separate surveys (F5000+B5000), which correspond to a total of 10000 deg^2 . This represents a cost saving of about a factor of 10, if we assume that cost scales with survey area. Also recall that F+B only uses RSD over B5000 and lensing over F5000, while FxB include all probes and all cross-correlations.

In the case of the PAU Survey, we find from photo-z simulations that the narrow-band filters also improve the photo-z accuracy of the Faint sample from $0.05(1+z)$ to about $0.03(1+z)$. If we include this improvement, the $\text{FoM}_{w\gamma}$ for FxB200 increases by another 30%.

6.4 Spectroscopic and Photometric combinations

Entries #20-21 of Table 7 shows that the FxB5000 combination are about 6-12 times larger $\text{FoM}_{w\gamma}$ than F+B (#17-18)), even when F+B correspond to twice the area (they come from independent surveys and therefore have twice as many independent modes). Part of this gain comes from the fact that in the FxB combination we have two probes (WL and RSD) to measure the bias of the B population, while for the F+B combination the bias in B is only measure with RSD. In principle one can also infer the bias of the B spectroscopic population by identifying the same bright population within the photo-z ($i_{AB} < 24$) sample and doing the cross-correlation of the faint and bright galaxies. This can improve the F+B result by a factor of 5, but is still a factor of 2 lower than FxB because of the larger photo-z errors.

This gain is illustrated in Fig.13, which shows the 3 projections (w_0, w_a, γ) in the $\text{FoM}_{w\gamma}$ ellipsoid. Alone, the RSD

results (purple) in the spectroscopic sample (B5000spec) are less powerful in constraining $\text{FoM}_{w\gamma}$ than Shear-Shear (blue), but the improvement resides in the complementarity of the combination to break degeneracies. This can be seen in the red contours (F+B5000spec) which combine both RSD and Shear-Shear assuming they are independent.⁸ When the B5000spec sample is a subset over the same area of the F5000 sample, we can also include all their cross-correlations and provide a second route to measure bias evolution. This benefits both WL and RSD, and the combination is over a factor of 15 larger (yellow FxB contours in the figure) than F+B and a factor of 10 times larger than all WL in the Faint sample alone (entry #4 in Table 7).

Figure 5 shows the corresponding result using MAG and RSD over 200 deg², instead of Shear and RSD over 5000 deg². In this case the gain in the combination FxB (see Table 3) is over a factor of 9 times larger than F+B and over 17 the one in MAG in the faint sample alone. The extra benefit here comes from the higher sampling rate in the PAUCam strategy.

The BAO+RSD (B5000highz) combination (entry #14) is comparable to the F+B5000 or the FxB200 combinations. BAO and RSD have also been used to constrain bias (e.g. see Amendola, Quercellini and Giallongo 2005, Cinzia, Amendola and Branchini 2011). But this is a factor of 5 lower than the WL-all+RSD independent combinations (#19) and a factor of 30 lower than the FxB cross-correlation result (#21). The results for B5000spec21.5 (last entry in the Table) are about a factor of 2 lower in the combined FoM than the corresponding $i_{AB} < 22.5$ result (#22).

6.5 Spectroscopic follow-up strategy

The WLxRSD (or MAGxRSD) strategy appears much better than doing a BAO approach over the same B5000 sample. The combination of WL and RSD produces a FoM_w about 24 larger than BAO alone over B5000. The reason is that in BAO we are ignoring the $P(k)$ amplitude and WL distance ratios information. In fact, RSD alone can give better or comparable FoM than BAO despite the additional biasing parameters. It also produces interesting constraints in γ which BAO cannot measure.

A potential advantage of a BAO follow-up would be to sample larger volumes as in B5000highz which corresponds to a selection of higher redshift targets out of F5000, with around 2000 galaxies/deg² with constant density per unit redshift between 0.2 and 1.7. This is shown in the #10 entry of Table 7. The improvement in FoM_w is significant but still far from the WL cases. The combination of BAO and RSD produces only a modest improvement over the BAO alone result, similar to MAG+RSD from separate surveys.

To have a fair comparison or optimization of which could be the best strategy (going deep as in B5000highz or shallower as B5000spec) we would need to add BAO to WL and RSD as separate probes (F+B). This is not totally straight forward as these probes could be correlated. Our

WL forecast already includes BAO wiggles (see §5.9). What we can do here is to combine the BAO measurement with WL and RSD, as if they were from independent samples. This is partially true as there is little volume overlap between B5000highz and B5000spec (where the lenses to F5000 reside). In any case, this is an upper bound of the true result, because the covariance between WL and BAO will lower the FoM. Results are shown as entries #15-16 in Table 7. The BAO+WL-all combination is similar to the RSD+WL-all combination. When we combine everything BAO+WL-all+RSD (entry #16) the outcome is of course higher than the WL+RSD combination (F+B). But it is still over a factor of 5 lower than the FxB WL-all+RSD cross-correlation (#21). This indicates that a shallower spectroscopic follow-up strategy provides better returns in terms of FoM. The legacy value of such spectroscopic follow-up could also be larger as we will be able to relate dark matter, as traced by WL, to galaxy formation, as traced by galaxies over the same structures.

7 CONCLUSION

In this paper we advocate the use of the cross-correlation of a deep (faint) photometric sample with a foreground brighter spectroscopic subset using narrow radial redshift bins. The foreground sample could also be photometric with very good photo- z of $\sigma_z/(1+z) \simeq 0.0035$. We consider three different types of probes in the analysis: 1) angular clustering from galaxy-galaxy autocorrelation in narrow redshift bins, 2) weak lensing (WL) from shear-shear, galaxy-shear and magnification (i.e. galaxy-galaxy cross-correlation), 3) redshift space distortions (RSD), from the ratio of transverse to radial modes. The combination of such measurements provides a significant improvement in the forecast for the evolution of the dark energy equation of state, given by $w(z)$, and the cosmic growth evolution, given by γ .

This improvement comes from the use of narrow redshift bins and the measurement of galaxy bias, which affects both RSD and WL cross-correlations, but in different ways. For transverse modes, biasing can be obtained by comparing WL clustering with galaxy angular clustering, but this is also degenerate with geometrical factors that depend on cosmic expansion evolution. In redshift space, bias can be measured directly by comparing line-of-sight to transverse clustering. The combination of both methods results in a very accurate determination of bias evolution, also breaking the degeneracy of growth with cosmic expansion evolution. We have shown that this gain is only fully accomplished when both WL and RSD measurements are done over the same area of the sky.

A new figure of merit, $\text{FoM}_{w\gamma}$, that encodes both cosmic expansion $w(z)$ and growth evolution γ is introduced to explore changes with the sample area, A , the redshift completeness, η , the magnitude limit of the bright sample, m_l , the photo- z or spectroscopic error, σ_z and the uncertainty in the fraction of photo- z transitions Δ_r defined in §3.12. For the magnification (MAG) and RSD combination over the same area (FxB) we find

⁸ If on top of S-S we also include G-S+G-G in the F5000 sample, the combined FoM increases by a factor 2 (entry #19).

$$FoM_{w\gamma} \simeq 2700 \bar{A}^{0.89} \eta^{0.22} 1.4^{m_l - 22.5} e^{-\bar{\sigma}_z^2 - \bar{\Delta}_r \bar{A}^{0.05}} \quad (95)$$

where \bar{A} is the survey area in units of 200 deg², m_l is the magnitude limit of the bright sample, $\bar{\sigma}_z$ is the photo-z error of the bright sample in units of 0.01(1+z) and $\bar{\Delta}_r$ is the absolute uncertainty in the fraction of photo-z transitions in units of 0.18. This can be used to extrapolate to values for different survey parameters within the ranges we have explored, i.e. $\bar{A} \in [1, 50]$, $\eta > 0.01$, $m_l \in [21.5, 23.0]$, $\bar{\sigma}_z < 0.7$ and $\bar{\Delta}_r < 0.6$. If we include all WL probes: shear-shear, galaxy-shear and magnification, the above $FoM_{w\gamma}$ is about a factor of 1.8 (3.1) times larger than Eq.95 for 200 (5000) deg². These results are robust and conservative. We only use linear scales ($k_{min} = 0.1$) and a relatively large redshift bin-width of $\Delta z \simeq 0.014(1+z)$. Better results can in principle be obtained using smaller scales and narrower redshift bins, but this requires further assumptions and modeling. We use a conservative modeling of biasing, which uses four parameters for each population (i.e. faint and bright subsamples) and no priors. With two bias parameters per population the above FoM increases by about 40%.

Shear-Shear alone (excluding galaxy bias and galaxy correlations) produces smaller FoM than magnification alone. Galaxy-Shear (including galaxy-galaxy autocorrelation and galaxy bias) can produce a factor 3 times better FoM_w than MAG (i.e. galaxy-galaxy cross and autocorrelation) because the latter is subject to larger sampling error from the background galaxy-galaxy autocorrelation. All WL probes benefit equally from the boost in the cross-correlation with RSD. They provide similar cosmological information (see Van Waerbeke 2009), so that the final FoM will depend on the size of systematic errors and the number density and volume that we can trace in each case. As illustrated by our results in Eq.95, magnification alone, without shape information, can be used to provide very competitive cosmological information.

We have not considered here photo-z bias or shear multiplicative or additive biases as they are more survey dependent and have been studied elsewhere (see Huterer 2006, Bernstein 2009 and references therein). But we have found new requirements on the uncertainties of photo-z transitions for the magnification, galaxy-shear and shear-shear probes to work. For all cases, the transitions r_{ij} (or photo-z contamination) needs to be known to about 1% (absolute error in r_{ij}) if we want only a small degradation in the $FoM_{w\gamma}$ (see Fig.12 and Eq.92). These values look within reach for future surveys. But note that as indicated by Eq.91, this requirement increases as $\ell_{max}^{1/2}$ where ℓ_{max} is the maximum multipole (or smaller angular scale) used in the fit. In our case we only use linear scales (Eq.13). A fit using non-linear scales ($\ell_{max} \simeq 6000$) needs to know photo-z transitions to 0.4% and also requires understanding of how baryonic physics could change the non-linear $P(k)$ (Van Daalen et al. 2011, Semboloni et al. 2011).

Given current limitations on systematics of shear measurements, specially for deeper ground based surveys, pushing for magnification as a cosmological tool is a good alternative to implement the WL+RSD cross-correlation advo-

cated here. A clear advantage for magnification would be to consider deeper photometric samples (such as LSST which can reach $r \simeq 27.5$, Ivezić, et al. 2011), where galaxy shapes are dominated by atmospheric noise but we can still measure magnitude and photo-z errors (see Van Waerbeke et al. 2010, Namikawa, Okamura & Taruya 2011). In this case, the magnification and RSD cross-correlation presented in this paper could play a significant role, provided we can perform an appropriate deep spectroscopic follow-up of the foreground lenses and provided we can calibrate the fraction of photo-z transitions. The PAUCam concept, based on doing photometric redshifts from 40 narrow (100Å) and 6 broad bands, seems well suited for such deep spectroscopic follow-up as we have found that the characteristic PAU photo-z error of $\sigma_z = 0.0035(1+z)$ only degrades the $FoM_{w\gamma}$ by $\sim 10\%$ (e.g. Fig.11 and Eq.95).

To design a spectroscopic follow-up survey of a photometric (WL) survey, we find that we can obtain 5 times better $FoM_{w\gamma}$ by targeting the foreground lenses to do cross-correlations, as proposed here, than trying to go deeper to measure BAO (compare entry #21 to #16 in Table 6), as has been proposed in several future surveys, such as Euclid, BigBOSS, HETDEX or FOCAS (WF MOS). Measuring BAO with a 5000 deg² PAU Survey (Benitez et al. 2009) provides 2-3 times smaller FoM_w than doing RSD+MAG (or WL) cross-correlation with the same PAUCam instrument over a much smaller 200 deg² area (compare #11-13 to #9 in Table 7). This represents a factor 50 to 75 improvement in profit over cost, defined as FoM achieved per unit area.

In our analysis we have only considered the gains in the photometric and spectroscopic cross-correlation using the 2-point clustering statistics. Higher order correlations will certainly add additional benefits both in the weak-lensing probes (e.g. see Gaztanaga & Bernardeau 1998, and references therein) and in galaxy biasing (Frieman & Gaztanaga 1994 and references therein). Besides the improvement in cosmological inference, the cross-correlations of spectroscopic and photometric surveys should also provide key information on the relation between galaxy evolution and dark matter growth, which will bring some new light into the problem of galaxy formation.

ACKNOWLEDGEMENTS

We would like to thank Benasque Center for Science for their great hospitality during the Cosmology 2010 workshop where the ideas in this paper were discussed and Anne Bauer, Gary Bernstein, Yan-Chuan Cai, Enrique Fernandez, Josh Frieman, Wayne Hu, Bhuv Jain, Antony Lewis and David Weinberg for discussions and feedback on ideas in this paper. Funding for this project was partially provided by the Spanish Ministerio de Ciencia e Innovacion (MICINN), project AYA2009-13936, Consolider-Ingenuo CSD2007- 00060, European Commissions Marie Curie Initial Training Network CosmoComp (PITN-GA-2009-238356), research project 2009-SGR-1398 from Generalitat de Catalunya and the Juan de la Cierva MEC program. The MICE simulations have been developed at the MareNostrum supercomputer (BSC-CNS) thanks to grants

AECT-2006-2-0011 through AECT-2010-1-0007. Data products are stored at the Port d'Informaci Cientfica (PIC).

REFERENCES

- Amendola L., Quercellini and Giallongo 2005, MNRAS, 357, 429
 Albrecht, A., et al. 2006, arXiv:astro-ph/0609591
 Bartelmann, M & Schneider, P., 2001, Phys.Rept. 340, 291
 Benítez, N., Gaztanaga, E., Miquel, R., Castander, F et al. 2009, ApJ 691, 241
 Benjamin J., Van Waerbeke L., Menard B, Kilbinger M. 2010, arXiv: 1002.2266
 Bernardeau, F., Colombi, S., Gaztañaga, E., & Scoccimarro, R. 2002, Phys.Rep., 367, 1
 Bernstein, G. 2009, ApJ 695, 652
 Bernstein G., Huterer D., 2010, MNRAS, 401, 1399
 Bernstein, G. & Jain, B. 2004, ApJ 600, 17
 Bernstein, G. , Cai, Y, 2011, arXiv:1104.3862
 Blanton M. R., et al., 2003, ApJ, 592, 819
 Bonoli, S, Pen, U.L., 2009, MNRAS 396, 1610
 Broadhurst, T.J., Taylor, A.N., Peacock, J.A. 1996, ApJ 438, 49
 Cabré, A., Fosalba, P., Gaztañaga, E., & Manera, M. 2007, MNRAS, 381, 1347
 Cabré A., Gaztañaga E., 2009, MNRAS, 393, 1183
 Casas, R. et al. 2010, SPIE, 7735, 36-11
 Casas-Miranda R., Mo H. J., Sheth R. K., Boerner G., 2002, MNRAS, 333, 730
 Challinor A., Lewis A., 2011, arXiv:1105.5292
 Chevallier M., Polarski D., 2001, IJMPD, 10, 213
 Cinzia, S., Amendola L., Branchini 2011, arXiv:1101.2453
 Coupon et al 2011, arXiv:1107.0616
 Croce M., Fosalba P., Castander F. J., Gaztañaga E., 2010, MNRAS, 403, 1353
 Croce M., Cabré A., Gaztañaga E., 2011, MNRAS, 414, 329
 Croce M., Gaztanaga E., Cabre A., Carnero A., Sanchez E., 2011, arXiv:1104.5236
 Dahlen T., Mobasher B., Somerville R. S., Moustakas L. A., Dickinson M., Ferguson H. C., Giavalisco M., 2005, ApJ, 631, 126
 Dahlen T., Mobasher B., Dickinson M., Ferguson H. C., Giavalisco M., Kretchmer C., Ravindranath S., 2007, ApJ, 654, 172
 Dekel A., Lahav O., 1999, ApJ, 520, 24
 Eisenstein, D. J., & Hu, W. 1998, ApJ, 496, 605
 Fang W., Hui L., Menard B., May M., Scranton R., 2011, arXiv, arXiv:1105.3421
 Fosalba, P., Gaztañaga, E., Castander, F., & Manera, M. 2008, MNRAS 391, 435
 Frieman J. A., Gaztanaga E., 1994, ApJ, 425, 392
 Fry, J, Gaztañaga E., 1993, ApJ 413, 447
 Gaztanaga E., Bernardeau F., 1998, A&A, 331, 829
 Gaztañaga & E., Lobo J.A., 2001, ApJ 548, 47
 Gaztañaga E., Norberg P., Baugh C. M., Croton D. J., 2005, MNRAS, 364, 620
 Gaztañaga E., 2003, ApJ 589, 82
 Gaztañaga E., Cabré A., Hui, L. 2009, MNRAS, 399, 1663
 Gaztañaga E., Miquel R., Sánchez E., 2009, PhRvL, 103, 091302
 Gunn, J. E. 1967, ApJ 147 61
 Guzik, J, Jain, B, Takada, M, 2010, PhR D, 81, 3503
 Hildebrandt, H., van Waerbeke, L., & Erben, T. 2009, A&A 507, 683
 Hikage C., Takada M., Spergel D. N., 2011, arXiv:1106.1640
 Hoekstra, H. et al. 2002, ApJ, 577, 604
 Hu, W. 1999, ApJ, 522, L21
 Hu, W.& Jain, B., 2004, PhR D, 70, 3009
 Hui L., Gaztañaga E., Loverde M., 2007, PhRvD, 76, 103502
 Hui L., Gaztañaga E., Loverde M., 2008, PhRvD, 77, 063526
 Huterer D., Takada M., Bernstein G., Jain B., 2006, MNRAS, 366, 101
 Ilbert O., et al., 2010, ApJ, 709, 644
 Ivezić, Z. et al. 2011, arXiv:0805.2366
 Jain, B. & Taylor, A. 2003, Phys.Rev.Lett., 91, 141302
 Jeong, D., Komatsu, E., 2006, ApJ, **651**, 619
 Jeong, D., Komatsu, E., 2009, ApJ, **691**, 659
 Johnston D. E., Sheldon E. S., Tasitsiomi A., Frieman J. A., Wechsler R. H., McKay T. A., 2007, ApJ, 656, 27
 Jouvel S., et al., 2009, A&A, 504, 359
 Kaiser, N. 1987, MNRAS, 227, 1
 Komatsu, E. et al. 2008, arXiv:0803.0547
 Linder, E. V. 2003, Phys.Rev.Lett. 90, 91301
 Linder, E. V. 2005, PhR D v72, 043529
 Loverde, M., Hui, L., & Gaztañaga, E. 2008, Phys.Rev.D, 77, 023512
 Loverde, M., & Afshordi, N. 2008, PhR D, 78, 123506
 Lue, A., Scoccimarro, R. and Starkman, G. 2004, PhR D 69, 044005
 Manera, M, Gaztañaga E., 2011, MNRAS 415, 383
 Manera, M, Sheth, R.K., Scoccimarro, R., 2010, MNRAS 402, 589
 Matsubara, T., 2004, ApJ 615, 573
 Menard, B, Scranton, R., Kukugita, M, Richards, G., 2010, MNRAS 405, 1025
 Moessner, R., Jain, B.,1998, MNRAS 294, L18
 McDonald, P, Seljak, U, 2009, JCAP 10, 007
 Narayan, R., 1989, ApJL 339, 53
 Namikawa, T, Okamura, T., Taruya, A., 2011, PhRv D, 83, 123514
 Newman J., 2008, ApJ 684, 88
 Nock K., Percival W. J., Ross A. J., 2010, MNRAS, 407, 520
 Peebles, P. J. E., The large-scale structure of the universe, Princeton, N.J., Princeton University Press, 1980. 435 p.
 Pen U.-L., 1998, ApJ, 504, 601
 Pogosian et al. 2011, arXiv:1002.2382
 Refregier A., 2003, ARA&A, 41, 645
 Refregier A., 2011, A&A, 528, 33
 Reyes et al. 2010, Nature, 464, 256
 Ross A. J., Percival W. J., Crocce M., Cabré A., Gaztañaga E., 2011, MNRAS, 415, 2193
 Scoccimarro R., Sheth, R., Hui, L., Jain, B. 2001, ApJ 546, 20
 Seo, J. J., Eisenstein, D. J. 2007, ApJ, 665, 14
 Scranton et al. 2005, ApJ, 633, 589
 Semboloni E., Hoekstra H., Schaye J., van Daalen M. P., McCarthy I. G., 2011, MNRAS, 1461
 Sefusatti, E., Crocce, M., Pueblas, S., Scoccimarro, R. 2006, PhR D 74, 023522
 Seljak, U, Warren, M., 2004, MNRAS 355, 129
 Song, Y, Zhao, G., Bacon, D., Koyama, K, Nichol, R., Pogosian L. arXiv:1105.2106
 Tegmark, M., Hamilton, A. J. S., Strauss, M. S., Vogeley, M. S., Szalay, A. S., ApJ, **499**, 555 (1998)
 Tegmark, M., Peebles, P.J.E., ApJL 500, L79
 van Waerbeke, L. 2009, MNRAS, 401, 2093
 van Waerbeke, L. Hildebrandt, H, Ford, J., Milkeraitis, M, 2010, ApJL, 723, L13
 van Daalen M. P., Schaye J., Booth C. M., Dalla Vecchia C., 2011, MNRAS, 415, 3649
 Villumsen, J., Freudling, W., da Costa, L.N., 1997, ApJ 481, 578
 White, M., Song, Y-S., Percival, W. J., MNRAS, **397**, 1348 (2009)
 Zhang, P., Liguori, M., Bean, R., Dodelson, S., 2007, PRL, 99, 141302